153

Modelling of cavitation in diesel injector nozzles

E. GIANNADAKIS, M. GAVAISES AND C. ARCOUMANIS

Centre for Energy and the Environment, School of Engineering and Mathematical Sciences,
City University, London, UK

A computational fluid dynamics cavitation model based on the Eulerian–Lagrangian approach and suitable for hole-type diesel injector nozzles is presented and discussed. The model accounts for a number of primary physical processes pertinent to cavitation bubbles, which are integrated into the stochastic framework of the model. Its predictive capability has been assessed through comparison of the calculated onset and development of cavitation inside diesel nozzle holes against experimental data obtained in real-size and enlarged models of single- and multi-hole nozzles. For the real-size nozzle geometry, high-speed cavitation images obtained under realistic injection pressures are compared against model predictions, whereas for the large-scale nozzle, validation data include images from a charge-coupled device (CCD) camera, computed tomography (CT) measurements of the liquid volume fraction and laser Doppler velocimetry (LDV) measurements of the liquid mean and root mean square (r.m.s.) velocities at different cavitation numbers (CN) and two needle lifts, corresponding to different cavitation regimes inside the injection hole. Overall, and on the basis of this validation exercise, it can be argued that cavitation modelling has reached a stage of maturity, where it can usefully identify many of the cavitation structures present in internal nozzle flows and their dependence on nozzle design and flow conditions.

1. Introduction

Current common-rail fuel injection systems for direct injection diesel engines operate at very high pressures, up to 1800 bar, while the whole injection process lasts for very short time intervals – of just a few milliseconds. The injection rate is controlled through the fast opening and closing of the needle valve, whereas the typical diameter of nozzle holes is 0.1–0.2 mm. As the flow from the injector enters into the nozzle discharge holes, it has to turn sharply from the needle seat area, which leads to the static pressure of the liquid at the entrance of the holes falling below its vapour pressure and initiation of cavitation. The occurrence of cavitation in orifices and its significant effect on spray formation have been known for quite some time. From the early experiments of Bergwerk (1959), using simplified large-scale and real-size single-hole acrylic nozzles, it was found that the discharge coefficient of the nozzle is mainly dependent on the cavitation number, which is a non-dimensional parameter indicating the expected cavitation intensity (see (1)), and is independent of the Reynolds number, i.e.

$$CN = \frac{p_{inj} - p_{back}}{p_{back} - p_{vapour}} \tag{1}$$

More recent experimental studies of the flow inside real-size and large-scale model nozzles have revealed the complexity of the two-phase flow structures formed over a

number of cavitation regimes; for example see Soteriou, Andrews & Smith (1995); Chaves *et al.* (1995); Arcoumanis *et al.* (1999). Other studies have revealed that cavitation significantly influences the atomization process of the emerging fuel, which represents one of the key factors affecting the performance and exhaust emissions of direct-injection diesel engines; e.g. see He & Ruiz (1995) and Tamaki, Shimizu & Hiroyasu (2001). Due to the difficulty in obtaining real-time measurements during the injection process, most of the reported experimental studies have employed devices operating under simulated conditions approaching those of diesel engines. Although very useful results have been obtained from large-scale nozzle experiments, e.g. see Soteriou, Smith & Andrews (1998); Afzal *et al.* (1999); Henry & Collicott (2000) and Roth, Gavaises & Arcoumanis (2002), the advances in instrumentation technology have allowed more information to be obtained in real-size injector nozzles. Such studies have been recently reported by Arcoumanis *et al.* (2000), Badock *et al.* (1999), Badock, Wirth &, Tropea (1999), Goney & Corradini (2000), Henry & Collicott (2000), Walther *et al.* (2000) and Blessing *et al.* (2003).

In contrast to the insight obtained from experimental studies such as the aforementioned ones, theoretical and modelling studies of nozzle flow cavitation were somewhat less forthcoming; an extensive coverage of the topic can be found in the review of Schmidt & Corradini (2001). One of the earliest efforts was reported by Delannoy & Kueny (1990), who employed a single-fluid mixture approach, combined with an empirical barotropic law model for the calculation of the mixture density variation as a function of pressure and the speed of sound. Two-dimensional simulations of cavitation in a Venturi nozzle have shown only qualitative rather than quantitative agreement with experiments. A similar two-dimensional model based on enthalpy considerations (Avva, Singhal & Gibson 1995) assumes thermal equilibrium between liquid and vapour and has shown acceptable agreement for the discharge coefficient dependency on cavitation number for nozzle holes with sharp inlet edges. In the barotropic law model of Schmidt, Rutland & Corradini (1997, 1999), cavitation was simulated by a continuous compressible liquid–vapour mixture, with the speed of sound, based on the homogeneous equilibrium model (HEM) of Wallis (1969). Although it was argued that compressibility is beneficial both physically and numerically, the authors have acknowledged that a drawback of barotropic models is the allowance of gradual density changes when gradual pressure gradients exist, which means that such models would not be easily applicable to large-scale lower-speed cavitation calculations, where there are very small pressure differences but quite steep density gradients. Another point about this approach is that it does not take into account turbulence effects. A similar model was also considered by Dumont, Simonin & Habchi (2001), who extended it to three dimensions. Another cavitation model developed and applied to simulations of diesel nozzles is that proposed by Marcer *et al.* (2000) and Marcer & LeGouez (2001), in which a volume-of-fluid (VOF) method was modified and combined with an energy-derived mass transfer model. The basic model assumption was that cavitation could be approximated by a larger-scale interface, which rules out the possibility of dispersed bubbles as observed in experimental studies. Although liquid compressibility was taken into account, turbulence modelling was not considered in their investigations.

In contrast to the cavitation models that are based on thermodynamic considerations, in which the pressure is considered only as a thermodynamic variable, there is a group of cavitation models that are based on the assumption that the pressure difference between the inner bubble and the surrounding liquid, acting as a mechanical force, is responsible for the appearance of cavitation. Furthermore, models whose basic

assumption is that cavitation occurs due to the growth of bubble nuclei belong to the same group. One of the early models in this category is that of Kubota, Kato & Yamaguchi (1992), although it has not been applied to nozzle flow simulations; in it, cavitation was treated as a viscous fluid whose density changed significantly due to the presence of vapour, with pure liquid and pure vapour treated as incompressible media. A bubble number density, which was assumed to be constant, and a local bubble radius were used to determine at each location the vapour fraction. The Rayleigh–Plesset (R-P) bubble dynamics equation expressed on a Eulerian frame of reference was used for calculating bubble growth and collapse; nevertheless, viscous and surface tension effects were not taken into account. Moreover, the behaviour inside the bubble was assumed to be isothermal, but possible existence of contaminant gas was not considered. In a similar effort by Chen & Heister (1996*a*, *b*) the number of bubble nuclei was assumed to be constant per unit mass of mixture. The flow inside single-hole diesel-like sharp-edged and rounded nozzles was simulated in two dimensions (Chen & Heister 1996*a*), and the above model was further validated (Bunnell *et al.* 1999) and extended to three dimensions in a single-hole geometry reminiscent of a diesel nozzle (Bunnell & Heister 2000). A similar model was developed by Grogger & Alajbegovic (1998) in which, although cavitation was considered as a mixture, the two-fluid method was employed; two sets of conservation equations were solved, one for the liquid phase and one for the vapour phase, allowing for a slip velocity. The mass transfer rate from one phase to the other was calculated by a simplified version of the classical R-P bubble dynamics equation, which is known as the Rayleigh or asymptotic equation; it assumes that the growth/collapse of bubbles depends solely on the difference between the liquid and the vapour pressures. Two- and three-dimensional simulations of venturi cavitating flows were performed. The model was able to reproduce the observed cavitation regimes, while the predicted pressure distribution agreed rather well with the experiment, although in terms of the vapour volume fraction there were significant differences. Subsequently, a revised version of the model was presented (Alajbegovic 1999; Alajbegovic, Grogger & Philipp 1999*a*, *b*), in which an empirical equation was used to account for the reduction of bubble number density with increasing vapour fraction. Variants of this bubble model were more recently presented (Sauer & Schnerr 2000; Schnerr & Sauer 2001), in which the classical interface-capturing VOF method was converted into a mixture model. In subsequent improvements to the initial approach the k-ω turbulence model was implemented (Yuan, Sauer & Schnerr 2000; Yuan & Schnerr 2001); predictions of cavitating flow in a single-hole sharp-edged nozzle showed that the inclusion of a turbulence model led to a steady-state solution, with no evidence of transient behaviour.

Another bubble-based model is that of Singhal *et al.* (2001, 2002), in which a mixture formulation was also followed, combined with the Rayleigh equation for vapour mass production/destruction. It should be pointed out that *ad hoc* coefficients and some empirical assumption about the maximum attainable bubble radius were employed, which effectively led to different equations for the evaporation and condensation rates. Simulations of steady-state cavitation through a sharp-edged orifice matched the dependence of the discharge coefficient on cavitation number, in agreement with the correlation of Nurick (1976). In contrast to the aforementioned bubble-based models, which were purely Eulerian, Sou, Masaki & Nanajima (2001) and Sou, Nitta & Nakajima (2002) utilized a Lagrangian frame of reference for the tracking of cavitation bubbles. However, in this investigation the researchers did not consider bubble dynamics; rather, in an arbitrary manner,

constant-diameter bubbles were introduced in the liquid, and when pressure reached a pre-selected value they were forced to collapse immediately. As a result, bubble breakup and coalescence could not be taken into account.

So far, no cavitation model has been presented which assesses the physical processes such as bubble nucleation, growth/collapse, breakup, coalescence and turbulent dispersion taking place in hole-type nozzles. Furthermore, past modelling studies have not considered the inherent stochastic nature of the phenomenon, evident in all experimental data available. As part of ongoing research on cavitation within the authors' group, numerous experimental data relevant to cavitation in diesel injectors have been presented (Arcoumanis *et al.* 1998; Arcoumanis *et al.* 1999; Arcoumanis *et al.* 2000; Roth, Gavaises & Arcoumanis 2002; Roth *et al.* 2005), together with early modelling efforts (Gavaises & Giannadakis 2004; Giannadakis *et al.* 2004). The stochastic flow processes incorporated into the developed model are thought to provide an improved theoretical framework relative to other models reported in the literature that adopted a thermodynamic or Eulerian–Eulerian approach for representing cavitation; this has been demonstrated in a recent study (Giannadakis *et al.* 2007) in which a comparison between cavitation models against experimental data, some of which are also used in the present study, has been performed.

This study aims to present the details of the complete form of this Eulerian–Lagrangian stochastic computational fluid dynamics (CFD) cavitation model and its application to diesel injector nozzles. The flow processes considered are described, and their relative importance is addressed, providing new physical insight into such flows. Special emphasis is given to detailed model validation against the in-house experimental data. These include CCD and high-speed images of the cavitation development in single- and multi-hole nozzles, LDV measurements of the liquid velocity as well as unpublished CT measurements of the cavitation volume fraction obtained in single-hole enlarged nozzles. In addition, cavitation images obtained in real-size nozzles incorporating transparent windows as well as measurements of the nozzle discharge coefficient have further been used for model validation. Finally, it is worth mentioning that extensions of the present model, linking cavitation with erosion and its application to new, emerging fuel systems for gasoline direct injection engines have been recently presented by Gavaises *et al.* (2007) and Papoulias *et al.* (2007), respectively, adding to the model's predictive capability over a wide range of applications and nozzle configurations.

In what follows the developed numerical model is described, highlighting the key assumptions and its applicability limits. Although it is not possible to validate independently each of the flow processes taking place in the subgrid time and length scales relevant to cavitation, the variety of the nozzle geometries and operating conditions tested have allowed macroscopic validation of the developed model, which has not been previously possible with existing models. The results from the numerous validation studies are then described followed by a summary of the most important conclusions.

2. Mathematical model formulation

In this section the developed model is described. Within the framework of the Eulerian–Lagrangian approach, cavitation is treated as a two-phase flow comprising the 'continuous' liquid and the 'dispersed' gas/vapour bubbles. The origin of cavitation is attributed to small bubble nuclei which are nucleated in the liquid after certain criteria are met and which grow once they experience steep depressurization.

Moreover, the cavitation bubbles interact with the flow, break up and coalesce and are transported through the surrounding liquid with non-zero slip velocity. All these processes are addressed by means of appropriate sub-models which are based on fundamental physical mechanisms developed independently elsewhere; they are, nevertheless, reported here for reasons of completeness and also for revealing their relative influence on the development of cavitation in hole-type nozzles, which is information relatively unknown from past studies. It can thus be argued that the described model does not simply bring together sub-models, which are readily able to predict cavitation without modifications or adjustments. Important aspects of the overall model performance include the numerical implementation of the various sub-models and the physical assumptions required to be made in order to predict the experimental observations. Most importantly, the numerical procedure established for the coupling between the Eulerian and the Lagrangian phases is of paramount importance, and also the treatment of the volume fraction of the cavitation bubbles, when they become larger than the numerical cells used for the discretization of the of liquid-phase equations, represents an important aspect of the developed model. A detailed presentation of the theoretical model is given next.

2.1. *Liquid-phase model*

For the liquid phase the volume- and ensemble-averaged continuity and Navier–Stokes equations are solved. As a result of the dynamic interaction of the cavitation bubbles with the surrounding pressure field, the available volume for the liquid phase can change significantly. This effectively means that, although the liquid phase is assumed to be incompressible, the actual flow at locations at which cavitation occurs can be regarded as compressible due to the fact that the velocity field does not have zero divergence due to the volume production/destruction caused by vapour. The effect of the vapour presence is taken into account by including the liquid-phase volume fraction α_L (referred to as liquid fraction) in the conservation equations. Moreover, due to the slip velocity between the cavitation bubbles and the flowing liquid, there is additional interaction, which is taken into account through the inclusion of the appropriate source terms in the conservation equations, i.e.

$$\frac{\partial}{\partial t}(\alpha_L \rho_L) + \nabla \cdot (\alpha_L \rho_L \boldsymbol{u}_L) = 0, \tag{2}$$

$$\frac{\partial(\alpha_L \rho_L \boldsymbol{u}_L)}{\partial t} + \nabla \cdot (\alpha_L \rho_L \boldsymbol{u}_L \otimes \boldsymbol{u}_L)$$
$$= -\nabla p + \alpha_L \nabla \cdot ((\mu_L + \mu_t)(\nabla \otimes \boldsymbol{u}_L + (\nabla \otimes \boldsymbol{u}_L)^T - \frac{2}{3}(\nabla \cdot \boldsymbol{u}_L)\boldsymbol{I})) + \boldsymbol{s}_{momentum}, \tag{3}$$

where $\boldsymbol{I}$ is the unit tensor and μ_t is the eddy viscosity calculated as

$$\mu_t = C_\mu \rho_L \frac{k_L^2}{\varepsilon_L}. \tag{4}$$

Since buoyancy effects were found to be negligible, the corresponding term in the momentum conservation equation has been dropped. In (3) through the term $\boldsymbol{s}_{momentum}$, the effect of the cavitation bubbles' relative motion upon the liquid phase is taken into account; its calculation is presented in a following paragraph, after the details of the cavitation bubbles model have been presented. Due to the fact that a model able to address the combined effect of turbulence and cavitation on the flow has as yet not appeared, and since nozzle flows are highly turbulent, the standard two-equation k-ε model has been employed for the consideration of turbulence effects. The transport

Constant	C_μ	$C_{\varepsilon 1}$	$C_{\varepsilon 2}$	$C_{\varepsilon 3}$	σ_k	σ_ε
Value	0.09	1.44	1.92	-0.33	1	1.3

TABLE 1. Coefficients in the standard k-ε mode.

equations for k and ε read as follows:

$$\frac{\partial(\alpha_L \rho_L k_L)}{\partial t} + \nabla \cdot (\alpha_L \rho_L \boldsymbol{u}_L k_L) - \nabla \cdot \left(\alpha_L \left(\mu_L + \frac{\mu_t}{\sigma_k} \right) \nabla k_L \right) = \alpha_L P - \alpha_L \rho_L \varepsilon + s_{kappa}, \quad (5)$$

$$\frac{\partial(\alpha_L \rho_L \varepsilon_L)}{\partial t} + \nabla \cdot (\alpha_L \rho_L \boldsymbol{u}_L \varepsilon_L) - \nabla \cdot \left(\alpha_L \left(\mu_L + \frac{\mu_t}{\sigma_\varepsilon} \right) \nabla \varepsilon_L \right)$$
$$= \alpha_L \frac{\varepsilon_L}{k_L} (C_{\varepsilon 1} P - C_{\varepsilon 2} \rho_L \varepsilon_L) + C_{\varepsilon 3} \alpha_L \rho_L \varepsilon_L \nabla \cdot \boldsymbol{u}_L + s_{epsilon}. \quad (6)$$

All the constants appearing in the above two equations have the standard k-ε model values (table 1). The terms s_{kappa} and $s_{epsilon}$ account for the additional effect of the bubbles' relative movement on the liquid-phase turbulent kinetic energy and its dissipation. Their calculation is based on the approach of Laín *et al.* (2002) and is presented in a following section. It has to be noted that, as part of the numerical tests that have been performed during the development of the model, a number of other two-equation turbulence models have been tested apart from the standard k-ε, namely the RNG of Yakhot *et al.* (1992) and the non-equilibrium version of Shyy *et al.* (1997); the latter has been applied in the simulation of cavitating flows (Vaidyanathan *et al.* 2003). Overall, it can be argued that although a variation of up to 3 % in the predicted nozzle discharge coefficient can be attributed to the turbulence model (Giannadakis *et al.* 2007), the details of the underlying physical processes are not affected significantly; furthermore, no model has been found to persistently predict cavitation better than the rest for all test cases, within the context of the Reynolds-averaged methodology. For this reason, it is considered that the model adopted here represents a robust engineering tool at the current state of the model's development and level of sophistication. Nevertheless, given the general shortcomings of two-equation turbulence models, it is expected that a more advanced modelling approach regarding turbulence, such as Reynolds-stress modelling and large-eddy simulation, will account for anisotropic effects and capture with enhanced temporal accuracy the fluctuating behaviour of the flow.

2.2. *Lagrangian cavitation model*

Within the context of the Lagrangian framework, it is necessary to simulate the large number of cavitation bubbles by means of a stochastic statistical approximation, based on the discrete bubble model (DBM) approach. Through this approximation, the total bubble population is represented by a number of parcels, each containing a large number of identical and non-interacting bubbles. The properties and some physical processes of these representative bubbles are randomly approximated from calculated distribution functions, using the Monte Carlo approximation, similar to the way that sprays are approximated with the droplet discrete model (DDM) method (see Dukowicz 1980). In order to describe statistically the total bubble population, a distribution function $f(\boldsymbol{x}, \boldsymbol{u}, R, t)$ is assumed that determines at time t the probable number of bubbles per unit volume located in the spatial range $(\boldsymbol{x}, \boldsymbol{x} + \mathrm{d}\boldsymbol{x})$, with

velocity in the range of $(\boldsymbol{u}, \boldsymbol{u} + \mathrm{d}\boldsymbol{u})$ and with radius in the range of $(R, R + \mathrm{d}R)$. For the conservation of the total number of bubbles in any volume of $(\boldsymbol{x}, \boldsymbol{u}, R, t)$ space moving with the bubbles, the following equation must be satisfied:

$$\frac{\partial f}{\partial t} + \nabla_{\boldsymbol{x}}(f \cdot \boldsymbol{u}) + \nabla_{\boldsymbol{u}}(f \cdot a) + \frac{\partial}{\partial R}(f \cdot \dot{R}) = \dot{f}_{Nucleation} + \dot{f}_{Breakup} + \dot{f}_{Coalescence}. \quad (7)$$

In the above equation, all the physical sub-processes that have been considered in the current model and have an effect on the distribution function f are included. Apparently, since thermal effects have not been taken into account, temperature T is not amongst the independent variables of (7). In order to solve the above equation, the Lagrangian approximation method has been used where the trajectory and momentum equations are solved for each individual bubble parcel. Subsequently, by employing single-bubble dynamics, the change of radius of each bubble parcel due to the surrounding liquid flow field is taken into account.

2.3. *Solution procedure*

The cavitation model can be used either for an unsteady simulation in a stagnant flow field or starting from an already-obtained single-phase solution. In the latter approach, one must allow for a sufficient number of time steps in order to obtain a pseudo-steady-state multi-phase solution. In this way one can assess the effect of cavitation on the flow, not only from a numerical but also from a physical perspective. Due to the different time scales inherent in the two phases, the selected tracking time step for the bubble phase Δt_B is much smaller than the corresponding one Δt_L for the continuous liquid phase. As a result, a number of sub-cycles are performed within the dispersed phase large enough to reach the time level of the continuous phase, which is subsequently calculated. The basic computational steps in the bubble phase can be summarized as follows:

1. Bubble nucleation on locations at which the pressure falls below the vapour pressure of the flowing liquid.

2. Calculation of new bubble location due to the initial velocity.

3. Interpolation of scalar and vector quantities from continuous liquid phase solution at the new location of the bubbles.

4. Computation of bubble momentum and dispersion.

5. Calculation of bubble dynamics, breakup and coalescence with the corresponding sub-models.

6. Estimation of void fraction due to the presence of the cavitating structures; calculation of the momentum and turbulence interaction source terms for the continuous liquid phase.

Some steps in this summary need to be explained in detail, since they posed a great challenge during the development of the current model, both from the conceptual and the numerical point of view.

2.3.1. *Bubble volume fraction calculation*

The coupling of the Eulerian continuous liquid phase with the Lagrangian dispersed bubble phase can become problematic if some inherent assumptions of the methodology are violated. The most important assumption of all Eulerian–Lagrangian methodologies is that the dispersed-phase volume fraction remains relatively low and that the typical dimensions of the parcels under consideration remain much smaller than the typical cell size of the Eulerian mesh. These assumptions can be violated in cavitating bubble flows, due to the combination of dense grids and the explosive growth of some bubbles that undergo large pressure drops. One should note that the
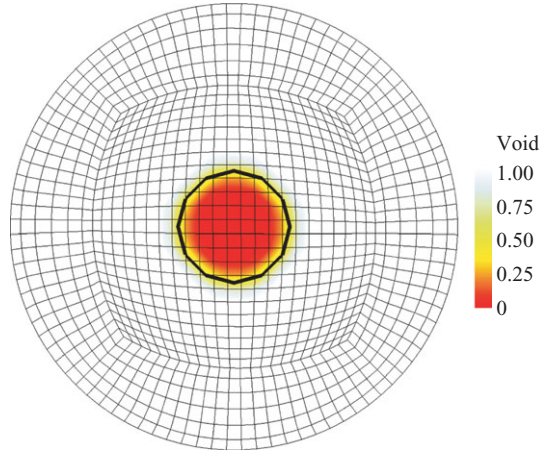
FIGURE 1. Bubble volume distribution in cells around the cell-containing parcel.

violation of the second assumption can take place not only for a Eulerian–Lagrangian bubble-based cavitation model but also in bubble-based Eulerian ones; this represents a universal theoretical weakness of this approach. In order to circumvent this limitation, a numerical methodology was developed in which the excess volume of each bubble parcel is distributed to its surrounding Eulerian cells. Normally, for the calculation of the volume fraction of a single bubble parcel α_B with a volume smaller than that of its host cell V_{cell} the following expression would suffice:

$$\alpha_B = \frac{1}{\Delta t_L V_{cell}} \int_t^{t+\Delta t_L} \frac{4}{3} \pi R^3 N \Delta t_B, \tag{8}$$

where N is the bubble number density of the parcel. With the above equation the time-averaged dispersed-phase volume fraction would be calculated for each cell, provided that the total volume of the bubble parcels present in this cell are smaller than the volume of the cell itself at all times. Time averaging is necessary due to the fact that the time step for the solution of each dispersed phase sub-cycle is usually much smaller than the time step for the continuous-phase solution, and so it is possible that parcels are transported through a number of cells during the sub-cycling part of the solution procedure. In order to account for this, during each dispersed phase sub-cycle the volume fraction of the bubbles is calculated for each cell; subsequently it is multiplied by the dispersed/continuous-phase time step ratio, $\Delta t_B/\Delta t_L$, and then it is integrated over all the dispersed-phase time steps. Nevertheless, in cavitating flows bubbles experience significant pressure drop within very short distance, which most of the time leads to their substantial expansion, and as a result the radius of some bubble parcels becomes larger than the host computational cell. In order to establish a conservative approach and address this problem, a special methodology has been developed; bubbles are allowed to grow larger than the cell they are occupying, but then the excess volume of the host cell is distributed to its adjacent ones. If any of the adjacent cells is already full of vapour, the distribution continues to the cells that are located further away, until all the excess volume is allocated. Once the distribution of the excess bubble volume is completed for all parcels, the volume fraction of the dispersed phase is calculated. From the dispersed-phase volume fraction, the continuous-phase void fraction is simply calculated as $\alpha_L = 1 - \alpha_B$. In figure 1 a cylinder is depicted, which has been discretized with a three-dimensional mesh. In

the centre of the cylinder a bubble is introduced, which is, large enough to fully enclose three cells across its radius. In the same graph the mesh and the void fraction on the middle plane of the cylinder are illustrated, together with the bubble under consideration; evidently, the successful distribution of the bubble volume is verified. It has to be noted that the method does not require specific cell geometry, since it can work with any polyhedral cell with arbitrary node location.

2.3.2. *Calculation of interphase source terms*

The physical interaction between the liquid and the cavitation bubbles due to their relative motion is taken into account in the current model through the concept of point source terms, an approach known as 'particle-in-cell' (Andrews & O'Rourke 1996). Within the context of this approach, the general form for the cell and the time-averaged momentum source term reads as follows:

$$\overline{S_{momentum}} = \int f(\boldsymbol{x}, \boldsymbol{u}, R, t) \rho_B \frac{4}{3} \pi R^3 N_{parcel} \frac{\mathrm{d}\boldsymbol{u}_{rel}}{\mathrm{d}t} \, \mathrm{d}\boldsymbol{x} \, \mathrm{d}\boldsymbol{u} \, \mathrm{d}R \, \mathrm{d}t, \tag{9}$$

where $\boldsymbol{u}_{rel} = \boldsymbol{u}_L - \boldsymbol{u}_B$ is the relative velocity between the two phases. In the above equation it should be mentioned that for cavitating flows buoyancy and latent mass effects have been neglected. Due to the sub-cycling process, the cell-based momentum source term $S_{momentum}$ is averaged temporally over the time step of the continuous phase Δt_L, similar to the calculation of the void fraction; the time averaging is denoted by the overbar. Once the source term is calculated from (9), it is introduced on the right-hand side of (3), the continuous-phase momentum equation. Although it is straightforward to estimate mathematically the interphase momentum exchange, when the focus changes to the effect of the dispersed phase on the turbulence of the continuous one, the opposite holds true. In the current study the approach of Laín *et al.* (2002) has been followed; within the context of this approach, a combination of the instantaneous and mean momentum source term with the dispersed- and continuous-phase velocities has been employed, leading to the following form for the turbulent kinetic energy source term:

$$S_{kappa} = \overline{\boldsymbol{u}_B \cdot \boldsymbol{S}_{momentum}} - \boldsymbol{u}_L \cdot \overline{\boldsymbol{S}_{momentum}}, \tag{10}$$

where the overbar again denotes temporal averaging over the dispersed phase sub-cycles. Having calculated S_{kappa}, the source term for the turbulence dissipation rate is approximated as

$$S_{epsilon} = C_\varepsilon \frac{\varepsilon_L}{k_L} S_{kappa}, \tag{11}$$

where C_ε is a model constant with a recommended default value of 1.8 (Laín *et al.* 2002).

2.3.3. *Modelling of bubble interaction with solid boundaries*

Another numerical aspect that has been developed and implemented in the present Eulerian–Lagrangian cavitation model is the approach adopted for the interaction of large bubbles with their surrounding solid boundaries. In cavitating flows, bubble expansion occurs very frequently in the vicinity of a solid boundary. Obviously, a bubble close to a wall should not be allowed to grow without any restriction; physically, the bubble should grow until its surface reaches the solid boundary. This is a point frequently overlooked in Eulerian models in which the bubble radius becomes a virtual variable, with a compromised physical meaning. Another issue that needs to be addressed with respect to large bubbles and solid boundaries is that of the

impingement of the former on the latter; normally, within the context of the classical modelling approach concerning the impingement of particles, droplets and bubbles, the necessary distance of the dispersed particle from the wall is calculated with respect to the particle's centre. Nonetheless, if the bubble radius is significant, i.e. comparable to the average grid cell size, the actual impingement point can no longer be the centre of the bubble; therefore, the numerical method that has been implemented identifies the actual contact point on the bubble surface with the adjacent three-dimensional solid surface boundary.

2.4. *Subgrid length scale and time scale cavitation bubble processes*

In this section, the various physical sub-models considered are described, and their relative influence on the flow development is evaluated; these include bubble nucleation, growth/collapse, breakup and collision/coalescence as well as bubble trajectory and associated effects of turbulence.

2.4.1. *Bubble nucleation*

It is well known that liquids are able to withstand considerable tension prior to the occurrence of cavitation (see e.g. Briggs 1950; Trevena 1987; Kinjo & Matsumoto 1998; Temperley & Trevena 1994; Xiao & Heyes 2002). In this case the inception of cavitation is attributed to the existence of microscopic nuclei, originating either from small crevices filled with contaminant gas and perhaps pure vapour present in the flowing liquid (heterogeneous nucleation) or from small voids in the liquid filled only with pure vapour (homogeneous nucleation). Extensive research has been carried out on the topic over the years by numerous groups (see e.g. Harvey *et al.* 1944; Fox & Herzfeld 1954; Apfel 1970; Kodama *et al.* 1981; Atchley & Prosperetti 1989; Rood 1991; Meyer, Billet & Holl 1992; Milton & Arakeri 1992; Vinogradova *et al.* 1995; Gindroz & Billet 1998; Liu & Brennen 1998; Arndt & Maines 2000; Mørch 2000; Hsiao, Chahine & Liu 2003). In the vast majority of engineering applications in which cavitation takes place, it can be argued that heterogeneous nucleation dominates, since all working fluids are expected to have a certain level of contamination and impurities. The currently proposed sub-model for free stream nucleation assumes microscopic spherical bubbles containing a random mixture of fuel vapour and contaminant gas; the latter is neglected in most of the Eulerian models. The majority of published experimental work on cavitating flows employs water as the working medium; for example see Meyer *et al.* (1992) and Liu & Brennen (1998). Both sets of measurements refer to natural and man-made environments, using water with different levels of contamination. The measured size distributions are quite scattered, exhibiting significant variance from each other. Clearly, this is an unavoidable and inherently stochastic behaviour which supports the argument for the development of a stochastic cavitation model. Given the lack of similar experimental data for diesel fuel and based on the fact that the above measurements essentially capture the level of water contamination that causes heterogeneous nucleation, it is assumed here that the contamination trends identified in water can be adopted for diesel fuel. Obviously, if homogeneous nucleation had been recognized as the dominant mechanism responsible for the inception of cavitation in diesel systems this assumption could not have been made. Observations of the measured nuclei size distributions from the aforementioned sources have resulted in an analytical linear fit, in double logarithmic scale, with which a probability density function (*pdf* hereafter)
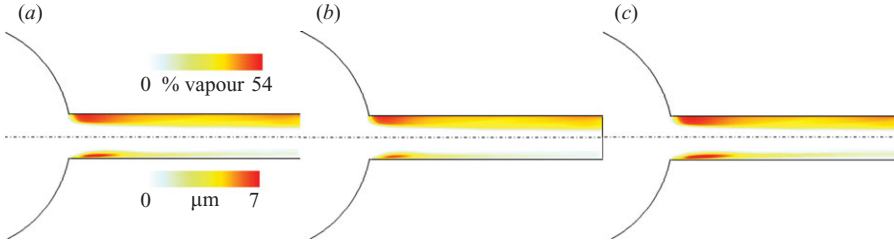
FIGURE 2. Effect of initial nuclei *pdf* on predicted cavitation volume percentage (top) and mean bubble size (bottom) spatial distribution inside the hole of the sharp-edged inlet single-hole nozzle using (*a*) logarithmic with $R_{min} = 0.1\,\mu m$ and $R_{max} = 1\,\mu m$, (*b*) logarithmic with $R_{min} = 0.01\,\mu m$ and $R_{max} = 1\,\mu m$ and (*c*) uniform with $R_{min} = 0.1\,\mu m$ and $R_{max} = 1\,\mu m$ ($p_{inj} = 500\,bar$; $p_{back} = 1\,bar$).

for the radius of the bubble nuclei can be formulated, i.e.

$$p(R) = \frac{n_{min}\left(\dfrac{n_{max}}{n_{min}}\right)^{\log\left(\frac{R}{R_{min}}\right)\big/\log\left(\frac{R_{max}}{R_{min}}\right)}}{\displaystyle\int_{R_{min}}^{R_{max}} n_{min}\left(\dfrac{n_{max}}{n_{min}}\right)^{\log\left(\frac{R}{R_{min}}\right)\big/\log\left(\frac{R_{max}}{R_{min}}\right)}\,\mathrm{d}R}. \tag{12}$$

The size range of the existing nuclei population, described by R_{min} and R_{max}, is assumed to be known, and it is an input to the model. Moreover, the number densities n_{min} and n_{max}, which correspond to the minimum R_{min} and the maximum R_{max} nuclei radii, need to be assumed as well. Typically, $n_{min} > n_{max}$, due to the lower probability of occurrence of larger nuclei. The above *pdf* has been termed logarithmic, and from this distribution function the radii of the newly created nuclei are randomly sampled. Comparison with experiments on real-size nozzles has led to the conclusion that nuclei formation should take place in areas in which the liquid pressure falls below the thermodynamic vapour pressure of the flowing liquid; this area will be referred to as volume 'under tension'. Apart from the location, the parameters affecting nucleation are the volume of the cell (probability p_{volume}), the liquid volume fraction (probability p_{void}) and the non-dimensional tension in the cell (probability $p_{tension}$). After all these parameters are estimated for each cell, the nucleation joint probability is calculated as

$$p_{cell} = p_{volume} \times p_{void} \times p_{tension}. \tag{13}$$

Numerical tests have revealed that modelling of the size *pdf* for the newly created nuclei does not represent an important element of macroscopic model predictions. These tests are conducted by performing two-dimensional simulations of the flow through a real-size sharp-edged single-hole planar nozzle; details for this nozzle are given in the next section. Here, it is only mentioned that it is a highly cavitating geometry, under realistic pressure conditions ($p_{inj} = 500$ bar and $p_{back} = 1$ bar) and that it is used as a test case for the presented parametric investigations. The effect of the initial radii *pdf* is confirmed in figure 2, where the predicted mean cavitation vapour-volume percentage and the arithmetic mean bubble size distributions within the hole of a sharp inlet (and thus cavitating) single-hole nozzle are presented. In these numerical tests, the logarithmic distribution function has been used with two different sets of initial radii; in figure 2(*a*, *b*) two nominal values for the minimum bubble size
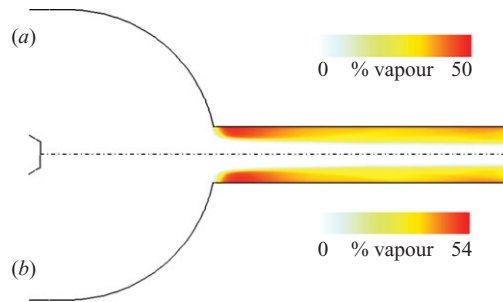
FIGURE 3. Effect of initial nucleus volume on predicted cavitation volume percentage inside the hole of the sharp-edged inlet single-hole nozzle using (a) 0.01 % and (b) 0.1 % ($p_{inj} = 500$ bar; $p_{back} = 1$ bar).

have been used, namely 0.1 and 0.01 µm, while in figure 2(c) a uniform distribution instead of the logarithmic one has been employed, with a nominal minimum radius of 0.01 µm. For all three cases, the maximum radius is 1 µm. It can be argued that this initial parameter, although it may be more influential in nozzles operating at very low cavitation numbers is, according to Giannadakis *et al.* (2007), not so critical for predictions in highly cavitating nozzles. This can be attributed to the initial explosive growth and the subsequent processes that the bubbles experience, which seem to be macroscopically independent from the very small initial nuclei size. Further numerical tests have revealed that the most influential parameter for model predictions is, rather than the assumed *pdf*, the initial volume percentage of the nuclei population at the time of creation relative to that of the flowing liquid which is under tension. Typically, the initial volume fraction ranges from 0.01 % to 0.5 % of the volume under tension. Results from a set of calculations performed with two different initial values of 0.01 % and 0.1 % can be seen in figure 3(a, b), respectively. Although an order of magnitude larger nuclei volume has been used, the predicted amount of cavitation vapour volume percentage has identical distribution with only a small difference in the peak value of less than 4 %. It should be mentioned that the effect on the predicted cavitation vapour volume fraction is not a linear function of the initial nuclei volume, and the outcome greatly depends on the specific nozzle design; fully cavitating nozzles are less sensitive to the assumed nuclei level, while for high-efficiency (tapered) nozzles or conditions of incipient cavitation, some dependency should be expected. Finally, as reported by Giannadakis *et al.* (2007), up to 2–3 % variation in the nozzle discharge coefficient could be expected for various initial nuclei populations over a wide range of nozzle designs considered in that study.

2.4.2. *Bubble dynamics*

In order to account for the growth and collapse of the bubble nuclei an improved version of the classical bubble dynamics approach has been pursued; improvements have been realized in order to account for bubble-to-bubble interactions and the combined effect of turbulence and the bubbles' slip velocity on the pressure they experience locally. It should be mentioned that some of the aforementioned theoretical studies have employed a reduced bubble dynamics model, namely the asymptotic or Rayleigh equation (Grogger & Alajbegovic 1998; Sauer & Schnerr 2000; Schnerr & Sauer 2001; Singhal *et al.* 2001, 2002). Unfortunately, this approach cannot capture some important aspects of the highly nonlinear behaviour of bubbles, since inertia effects on bubble response are discarded. Moreover, the important effect of the

contaminant gas and the less important surface tension and viscous effects are also ignored in studies that account for inertia effects (Kubota *et al.* 1992; Chen & Heister 1996*a, b*). Noticeably, as was pointed out in Chen & Heister (1996*a*), with reduced nozzle size the inertia effects on bubble dynamics become more important, leading to substantial non-equilibrium hydrodynamic effects. This explains why some of the Eulerian cavitation models utilize empirical coefficients in order to differentiate vapour production from the vapour destruction rate (Singhal *et al.* 2001, 2002). Furthermore, concerning the model description, due to the classical bubble dynamics framework the inherent assumptions are that cavitation bubbles remain spherical at all times and are surrounded by incompressible liquid. Given the omission of thermal effects from the analysis, the classical R-P equation for the radial motion of the bubble wall (Plesset & Prosperetti 1977; Brennen 1995) has been extended to the subgrid-scale (SGS) bubble interaction approach of Kubota *et al.* (1992):

$$\frac{p_V - p_\infty(t)}{\rho_L} + \frac{p_{G0}}{\rho_L} \left(\frac{R_0}{R}\right)^{3k} = R\ddot{R} + \frac{3}{2}\dot{R}^2 + \frac{4\mu_L}{\rho_L R}\dot{R} + \frac{2\sigma_L}{\rho_L R}$$
$$+ 2\pi\Delta r^2 \left(\dot{n}_{bub}^* \dot{R}R^2 + n_{bub}^* \ddot{R}R^2 + 2n_{bub}^* R\dot{R}^2\right), \quad (14)$$

where p_∞ is the far-field pressure in the liquid; p_V is the vapour pressure and p_{G0} the initial partial pressure of the contaminant gas inside the bubble; Δr is the radius of the assumed spherical cluster of interaction; and n_{bub}^* is the number of bubbles contained in the parcel under consideration divided by the host cell volume. All the liquid-phase properties, namely density ρ_L, dynamic viscosity μ_L and surface tension σ_L, are considered to be constant. For the exponent in the above equation, if $k = 1$ it implies that the bubble content behaves isothermally, and if $k = \gamma$ it implies that the behaviour of the bubble content is adiabatic, since γ is the polytropic coefficient. In the present case the criterion suggested by Moss, Levantin & Szeri (2000) has been adopted, which is based on the kinetic theory and enables the consideration of both thermal states within the bubble, depending on the instantaneous bubble wall velocity. If the following expression holds true, then there is isothermal behaviour inside the bubble ($k = 1$), i.e.

$$4X_0 \left(\frac{R}{R_0}\right)^{3(3-\gamma)/2} > R|\dot{R}|, \quad (15)$$

and for the opposite case $k = \gamma$; in the above equation X_0 is the thermal diffusivity of the contaminant gas at ambient temperature. The initial partial pressure p_{G0} is estimated by the following equation, assuming mechanical equilibrium:

$$p_{G0} = p_{\infty,t=0} - p_V + \frac{2\sigma_L}{R_0}. \quad (16)$$

The dynamics of a single bubble can be affected by other flow parameters as well. Due to the local liquid turbulence the pressure around a bubble is subjected to fluctuations, which leads to the instantaneous pressure experienced by the bubble becoming much lower than the mean pressure, if the magnitude of the fluctuations is quite high (Hinze 1975). Moreover, the pressure that is experienced by the flowing bubble can be lower than the average liquid pressure due to the slip velocity between the surrounding liquid and the bubble itself (Hsiao, Chahine & Liu 2000). In order to improve the validity of the Lagrangian approach, the 'far field' pressure used for the calculation of the dynamics of each bubble is not the one interpolated at its centre
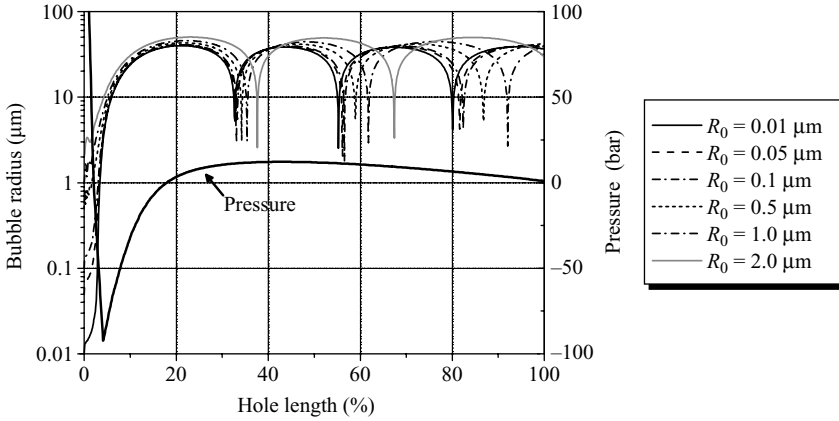
FIGURE 4. Predicted bubble size history along the length of the sharp-edged single-hole nozzle ($p_{inj} = 500$ bar; $p_{back} = 1$ bar).

but rather the average within the aforementioned cluster of influence. This leads to the following equation for the 'effective far field' pressure $p_\infty(t)$:

$$p_{\infty, effective}(t) = p_{\infty, aver}(t) - C_E \tfrac{2}{3}\rho_L k_L - \tfrac{1}{4}\rho_L |\boldsymbol{u}_L - \boldsymbol{u}_B|^2, \qquad (17)$$

where C_E is the Egler coefficient with a value of 1.2 (Hinze 1975), and k_L is the local turbulent kinetic energy in the surrounding liquid. The effective pressure $p_{\infty, effective}(t)$ is used in this equation in the place of $p_\infty(t)$; it should be noted at this point that the effect of relative velocity is much less important than the effect of local turbulence. For the numerical integration of (14) the explicit fifth-order Runge–Kutta–Fehlberg method (Press *et al.* 1992, 1996) has been employed. The algorithm used also features an embedded fourth-order Runge–Kutta method which makes it possible to obtain an estimate of the local integration error due to the truncation of the Taylor series expansion and adjust the local integration time step depending on the prescribed level of numerical accuracy. Examples of the bubble size history within the injection hole of a cavitating single-hole nozzle can be seen in figure 4. In these predictions the effect of the surrounding nozzle hole wall on the dynamics of the bubbles is neglected. The pressure experienced by the bubbles, as they travel along the injection hole and which causes this dynamic response, is also indicated in the figure; it has been extracted from a single-phase simulation. Results are presented for bubbles having an initial radius ranging from 0.01 to 2 µm. It is interesting to note that in the absence of a surrounding solid boundary and without taking into account bubble breakup or coalescence which may affect the nonlinear response of the bubble radius to the external pressure, the bubbles grow and collapse a few times before reaching the hole exit. Since the overall cavitation volume fraction is calculated instantly as a function of this rapidly changing bubble size, it becomes clear that accounting for all terms in the R-P equation is essential for model predictions. Comparing the curves plotted, it becomes clear that although some differences exist between them, the bubble size reaches a peak value which is not highly dependent on the initial size. Figure 5 shows the spatial distribution of the time-averaged bubble growth and collapse rates. It can be seen that most growth takes place at the hole inlet, although few bubbles are predicted to grow along the top part of the injection hole until its exit. On the contrary, a strong collapse zone is predicted just downstream of the hole entrance,
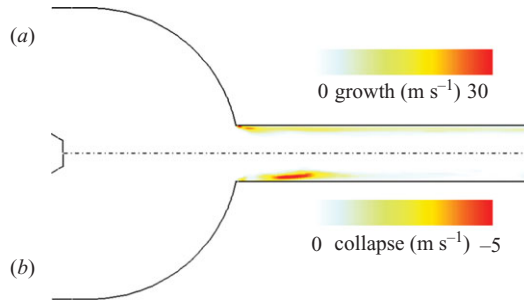
0 growth (m s^{-1}) 30

0 collapse (m s^{-1}) −5

(b)

FIGURE 5. Predicted temporally averaged (a) bubble growth and (b) bubble collapse rates inside the injection hole ($p_{inj} = 500$ bar; $p_{back} = 1$ bar).

following the initial bubble growth. It is of interest to note that this zone is not just at the hole inlet but further inside the injection hole; as has been reported in Gavaises *et al.* (2007), this region can be associated with the observed wall erosion and material loss caused by the sudden collapse of the cavitation bubbles.

2.4.3. *Bubble breakup and coalescence*

One of the assumptions made by classical bubble dynamics is that bubbles retain their sphericity throughout their lifetimes. In reality, bubbles deform due to the surrounding non-uniform pressure distribution and hydrodynamic forces acting upon them. This bubble deformation can result in bubble breakup, from which two or more smaller bubbles can emerge and which alters the behaviour of the bubble population, since 'daughter' bubbles behave differently due to their different dynamics after breakup with respect to the 'mother' bubble. Therefore, two primary mechanisms responsible for bubble breakup have been accounted for, namely turbulent breakup and hydrodynamic breakup. For the modelling of turbulence-induced bubble breakup, the work of Martínez-Bazán, Montañés & Lasheras (1999a, b) has been followed; this approach is based on purely kinematic arguments and has shown good agreement with measured data obtained from experiments in which relatively large bubbles are immersed in a turbulent flow, which is locally isotropic and homogeneous, and experience no shear due to slip velocity with the continuous liquid. Under these conditions bubble breakup can be attributed to the turbulence-induced shear acting upon them. Within the context of this model, the initial bubble size D_0 is assumed to lie within the inertial sub-range, $\eta < D_0 < L_x$, where η is the Kolmogorov micro-scale of viscous dissipation of local turbulence, and L_x is the integral length scale. Following Kolmogorov's universal theory for the estimation of the local velocity fluctuations (Batchelor 1953; Martínez-Bazán *et al.* 1999a) the critical bubble diameter D_c is defined as

$$D_c = 1.26 \left(\frac{\sigma_L}{\rho_L} \right)^{0.6} \varepsilon_L^{-0.4}. \quad (18)$$

Bubbles with a diameter smaller than the critical one can sustain turbulent stresses without breaking up. Given that a bubble has diameter $D_0 > D_c$, any two points on its surface separated by distance D' such that $D_{min} < D' < D_0$ will experience turbulent stresses sufficient to cause breakup of the bubble. D_{min} is calculated by equating the surface energy of a bubble with diameter D_0 to the deformation energy between

points at a distance D_{min} apart, which results in the following equations:

$$D_{min} = 1.77 \left(\frac{\sigma_L}{\rho_L D_0} \right)^{1.5} \varepsilon_l^{-1} \quad \text{or} \quad D_{min} = \eta, \quad \text{if} \quad 1.77 \left(\frac{\sigma_L}{\rho_L D_0} \right)^{1.5} \varepsilon_L^{-1} < \eta. \quad (19)$$

It is clear from the above equation that the smallest possible daughter bubble has size D_{min}; the largest possible size D_{max} for the daughter bubble is calculated from conservation of the 'mother' bubble volume. Within the framework of the adopted model it is assumed that only binary bubble breakup can take place. As for any mechanical process, it has been postulated that the rate at which breakup occurs is inversely proportional to the difference between the deformation and confinement forces. Furthermore, the breakup rate of a bubble with $D_0 < D_c$ ought to be zero. If t_{br} is the time that elapses before bubble breakup takes place, then the frequency g of bubble breakup is its reciprocal (Martínez-Bazán et al. 1999a):

$$g_{br,turb}(\varepsilon_L, D_0) = \frac{1}{t_{br,turb}(\varepsilon_L, D_0)} = \frac{0.25 \sqrt{8.2(\varepsilon_L D_0)^{2/3} - 12\sigma_L/\rho_L D_0}}{D_0}. \quad (20)$$

Apart from determining the breakup frequency due to turbulent stresses, one needs to know what is the resulting size of the emerging daughter bubbles. In the second part of the original work (Martínez-Bazán et al. 1999b), a *pdf* for the daughter bubble size could be formulated based on energy principles:

$$f^*(D^*) = \frac{P(D^*)}{\int_0^1 P(D^*)} = \frac{\left[D^{*2/3} - X^{5/3} \right] \left[(1 - D^{*3})^{2/9} - X^{5/3} \right]}{\int_{D^*_{min}}^{D_{max}} \left[D^{*2/3} - X^{5/3} \right] \left[(1 - D^{*3})^{2/9} - X^{5/3} \right] \mathrm{d}(D^*)}, \quad (21)$$

where $D^* = D_1/D_0$, $D^*_{min} = D_{min}/D_0$, $D^*_{max} = D_{max}/D_0$ and $X = D_c/D_0$.

Apart from the turbulence-induced shear, bubbles can break up due to the significant slip velocities between the dispersed bubbles and the continuous liquid phase. During the initial stages in the development of the current model it became obvious that such slip velocities can become quite significant in nozzle flows, and to account for this effect, a simple model based on the Weber number was followed. The Weber number, *We*, is defined here as:

$$We = \frac{\rho_L D |\boldsymbol{u}_B - \boldsymbol{u}_L|^2}{\rho_L}, \quad (22)$$

where $\boldsymbol{u}_B - \boldsymbol{u}_L$ is the relative velocity between the dispersed bubble and the continuous liquid; breakup is assumed to occur when $We > 12$. In order to calculate the resulting daughter bubble size from the breakup process, a maximum entropy formalism has been used (Ahmadi & Sellens 1993). Within the context of this approach and in the absence of any solid mathematical model that can describe daughter sizes from such a breakup process, it is assumed that the size *pdf* of the emerging bubbles ought to maximize the Shannon entropy defined as

$$S = - \int_{D^*_{min}}^{D^*_{max}} pdf(D^*) \ln[pdf(D^*)] \, \mathrm{d}D^*. \quad (23)$$

Another important phenomenon that takes place in such flows is bubble coalescence. The implementation of a coalescence sub-model has been pursued as a further enrichment of the current bubble-based approach which aims to make the model

applicable to densely cavitating flows. It is known that there is limited time available for bubble-to-bubble interactions that can lead to coalescence; moreover, when two bubbles approach each other, a liquid film is formed between them which tends to resist any further movement that could bring these bubbles even closer. Coalescence will occur only if the intervening film can drain to a sufficiently small thickness and rupture in the time available. With respect to coalescence in cavitating flows, there are two sources of relative bubble motion that are of particular interest: (a) motion induced by local turbulence in the continuous liquid and (b) motion induced by mean relative velocities between the bubbles. In some cases bubbles, although much larger than the Kolmogorov eddies, are smaller than the energy-containing eddies and for this reason in those flows source (a) is expected to be the dominant source of relative bubble motion (Kamp *et al.* 2001). Nevertheless, in the current approach both sources have been considered and implemented in the coalescence sub-model with a stochastic formulation, through which the most probable of the two mechanisms is selected. For the estimation of the interaction time t_i the approach of Kamp *et al.* (2001) has been followed here:

$$t_i = \frac{\pi}{4} \left(\frac{\rho_L C_{AM} D_{eq}^3}{3\sigma_L} \right)^{1/2}, \tag{24}$$

where D_{eq} is an equivalent bubble diameter defined by

$$D_{eq} = \frac{2 D_1 D_2}{D_1 + D_2}, \tag{25}$$

and C_{AM} is the added mass coefficient which depends on D_1 and D_2 and whose analytic expression can be found in Kamp *et al.* If bubble deformation had not been taken into account, the above-added mass coefficient could have been approximated with the typical value of 0.5.

Another important modelling detail is the calculation of the film drainage time t_d, which has been the subject of many theoretical studies. One of these was performed by Chesters & Hofman (1982), who obtained a numerical solution for the film drainage time by employing the assumption that the approach velocity of the two bubbles remains constant. A key parameter to the whole process is the equivalent film Weber number:

$$We_{eq} = \frac{\rho_L V_{rel}^2 D_{eq}}{2\sigma_L}, \tag{26}$$

where V_{rel} is the relative velocity between the two bubbles. For small Weber numbers the approximation of a constant approach velocity is an acceptable one, since for most cases $t_d \ll t_i$. Following again Kamp *et al.* (2001), the film drainage time is

$$t_d = k_1 \frac{\rho_L V D_{eq}^2}{8\sigma_L}, \tag{27}$$

where k_1 is a correction coefficient that accounts for finite Weber number effects and has a recommended value of 2.5. The coalescence probability is defined as

$$p_{coalescence} = e^{-t_d/t_i}, \tag{28}$$

which allows the outcome of a binary bubble collision to be evaluated. As mentioned previously, there are two primary driving mechanisms for bubble collisions: liquid turbulence and gradients in the mean bubble velocities. In order to decide which of the above two mechanisms prevails for each pair of bubble parcels, a stochastic

approach is followed. First, the collision frequency of each pair of bubble parcels, due to both mechanisms, is calculated. For turbulence-driven collisions, the frequency with respect to a parcel containing N_1 bubbles is calculated from the following expression (Kamp *et al.* 2001):

$$f_{turb} = \sqrt{\frac{8\pi}{3}} \frac{N_1 N_2}{V_{p1} \alpha_{L1}} (R_1 + R_2)^2 V_{turb}, \tag{29}$$

where N_1 and N_2 are the number of bubbles in each of the two involved bubble parcels; V_{p1} is the volume of the computational cell in which parcel N_1 is located; α_{L1} is the liquid fraction in this cell; and V_{turb} is the turbulence-induced relative velocity between the two parcels, which is calculated from the following equation:

$$V_{turb} = \frac{(\varepsilon_L (R_1 + R_2))^{1/3}}{\sqrt{2C_{AM}}}, \tag{30}$$

where ε_L is the average turbulence dissipation rate, calculated from the corresponding values at the two parcel locations. The frequency of the collisions driven by relative velocity is calculated from the following equation:

$$f_{urel} = \frac{\pi N_1 N_2}{V_{p1} \alpha_{L1}} (R_1 + R_2)^2 V_{rel}. \tag{31}$$

The probability of no collision taking place due to the relative velocity can be first estimated through the following equation:

$$p_{nocollision,urel} = e^{-f_{urel} \Delta t_B / N_{large}}, \tag{32}$$

where $N_{large} = Max(N_1, N_2)$. Subsequently, a random number r_{rel} is sampled from the uniform distribution function; if $r_{rel} > p_{nocollision,urel}$, then only collisions of this type are considered, and it is assumed here that relative velocity collisions have hierarchical priority. However, if $r_{rel} < p_{nocollision,urel}$, then the probability of turbulence-driven collisions taking place is also evaluated using the following equation:

$$p_{collision,turb} = f_{turb} \Delta t_B. \tag{33}$$

A uniform distribution random number r_{turb} needs to be sampled again; if $r_{turb} < p_{collision,turb}$ a turbulence-induced collision takes place, otherwise there is no collision at all. Once it is established that a collision will indeed occur, the outcome of the collision is decided by means of (28).

Since previously published cavitation models do not include such effects, it has been considered useful to present predictions obtained with and without the introduction of these physical processes. Figure 6 shows the predicted cavitation vapour volume percentage and the arithmetic mean bubble size spatial distributions inside the hole of the sharp-edged nozzle at fully cavitating conditions. Predictions are shown first without considering these effects (figure 6a), then by considering only breakup and neglecting bubble coalescence (figure 6b) and finally by considering both processes (figure 6c). It is clear that the predicted flow regime is strongly affected by the breakup process. When both effects are neglected, the cavitation cloud formed initially near the hole entrance has relatively large-sized bubbles which then fully collapse without reaching the hole exit. On the contrary, when the process of bubble breakup is considered, bubbles subsequently break down to much smaller sizes. Further growth is then suppressed due to the low value of the re-initialization pressure inside them, since after breakup (16) is used locally, in order to assign the bubble mechanical equilibrium conditions; the end result is a cavitation cloud which reaches the hole
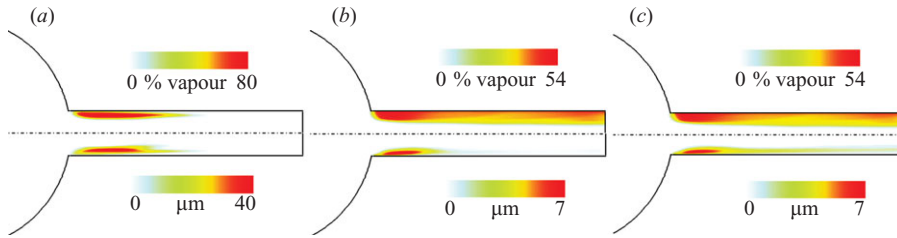
FIGURE 6. Effect of breakup and coalescence models on the predicted cavitation volume percentage (top) and mean bubble size spatial distribution (bottom) inside the hole of the sharp-edged inlet single-hole nozzle (*a*) using no breakup and coalescence (*b*) with breakup and no coalescence and (*c*) with breakup and coalescence ($p_{inj} = 500$ bar; $p_{back} = 1$ bar).
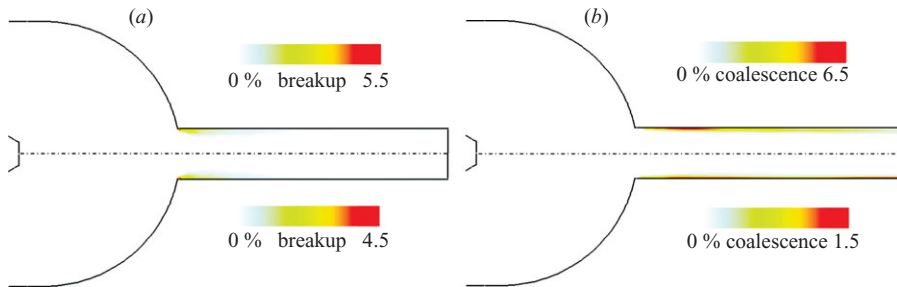

FIGURE 7. Predicted spatial distribution of percentage of bubbles (*a*) breaking-up and (*b*) coalescing along the injection hole, considering non-zero slip (top) and zero slip velocities (bottom) between the two phases ($p_{inj} = 500$ bar; $p_{back} = 1$ bar).

exit. Experimental results to be presented in the following section confirm that this two-phase flow regime does take place for this particular operating condition. The effect of bubble coalescence seems to be smaller compared to the effect of breakup, as can be seen by comparing the predicted distributions of figure 6(*b*, *c*). Further insight into the turbulent versus the hydrodynamic breakup and coalescence mechanisms is provided in figure 7, where the percentage of the bubbles breaking-up and coalescing is presented, with and without the slip velocity between the two phases. These results indicate that most bubbles break due to turbulent breakup, while the opposite holds true for bubble coalescence, where the relative velocity is the main cause for bubbles coalescing. It is also interesting to note that breakup phenomena mainly take place near the hole inlet which is the region in which high turbulence levels are present. At the same time, this is the region of bubble growth and collapse, which explains the profound effect on the predicted hydrodynamic regime when considering this process. On the contrary, bubble coalescence may take place along the entire hole length. Finally, it ought to be mentioned that although the number of bubbles actually breaking up or coalescing is in the range of 1–7 %, their volume represents up to 60 % of the total cavitation volume fraction.

2.4.4. *Single-bubble motion equation*

The last two sub-models considered account for the bubble velocity calculation and the response of the bubble to liquid turbulence. Following the single-point particle approximation (Michaelides 1997, 2003; Maxey & Riley 1983), the equation of motion for a single bubble is formulated after all the forces acting upon it are added. Since the mass of the bubble itself is negligible, bubble inertia is neglected,

which implies that the sum of all forces acting upon the bubble should be zero at all times (Johnson & Hsieh 1966; Tamura, Sugiyama & Matsumoto 2001), i.e.

$$
\frac{1}{2}C_D\rho_L\pi R^2(\boldsymbol{u}_L - \boldsymbol{u}_B)|\boldsymbol{u}_L - \boldsymbol{u}_B| + C_A\rho_L\frac{4}{3}\pi R^3\left(\frac{\mathrm{D}\boldsymbol{u}_L}{\mathrm{D}t} - \frac{\mathrm{d}\boldsymbol{u}_B}{\mathrm{d}t}\right)
$$

$$
-\frac{4}{3}\pi R^3\nabla p - \frac{4}{3}\pi R^3\rho_L\boldsymbol{g} + \frac{1}{2}C_l\rho_L\pi R^2|\boldsymbol{u}_L - \boldsymbol{u}_B|^2
$$

$$
\times \frac{(\boldsymbol{u}_L - \boldsymbol{u}_B)\times\omega_L}{|\boldsymbol{u}_L - \boldsymbol{u}_B||\omega_L|} + 2\pi\rho_L R^2(\boldsymbol{u}_L - \boldsymbol{u}_B)\frac{\mathrm{d}R}{\mathrm{d}t} = 0. \tag{34}
$$

The forces considered in the above equation are the drag, the added mass, the pressure gradient, buoyancy, lift and the volume variation force. The last appears essentially due to the added mass effect and is important for bubbles whose volume changes significantly with time during their motion (Johnson & Hsieh 1966). The Basset force has not been considered here following the finding of Meyer *et al.* (1992). For the drag force coefficient the approach of Feng & Michaelides (2001) has been followed; i.e. for Reynolds numbers in the range of $0 \leqslant Re_B \leqslant 5$ we have

$$
C_D = \frac{16}{Re_B}(1 + 0.1Re_B) - 0.02Re_B\ln(Re_B), \tag{35}
$$

and in the range of $5 < Re_B \leqslant 1000$,

$$
C_D = \frac{48}{Re_B}\left(1 + \frac{2.21}{\sqrt{Re_B}} - \frac{2.14}{Re_B}\right). \tag{36}
$$

The Reynolds number here is defined as $Re_B = 2R|\boldsymbol{u}_L - \boldsymbol{u}_B|\rho_L/\mu_L$. After the drag coefficient for a single bubble is calculated from (35) or (36), the 'dense-flow' correction of Rusche & Issa (2000) is applied, where

$$
C_D = C_{D,single\ bubble}\left(\mathrm{e}^{3.64(1-\alpha_L)} + (1-\alpha_L)^{0.864}\right). \tag{37}
$$

The above correction addresses the fact that the drag force exerted upon a group of bubbles is expected to be quite different than that which a single bubble would experience. The presence of other bubbles distorts the surrounding flow field in such a way that increased drag forces are exerted upon each one of them. In strongly cavitating flows, high vapour fraction values are expected, which implies the presence of a dense population of bubbles. A similar effect takes place with respect to the added mass phenomenon; for this reason an analogous correction to the added mass force of van Wijngaarden (1976) has been adopted:

$$
C_A = 0.5 + 1.39(1 - \alpha_L). \tag{38}
$$

Effectively, what this correction highlights is that the added mass effect on each bubble is augmented by the presence of other bubbles. For the lift force coefficient the formula proposed by Sridhar & Katz (1995) has been employed, where the vortex-induced lift force is considered, which can be much higher than the shear-induced lift force, i.e.

$$
C_l = 0.59\left(\frac{|\omega_L|R}{|\boldsymbol{u}_L - \boldsymbol{u}_B|}\right)^{1/4}. \tag{39}
$$

For the calculation of the new bubble velocity, (34) is rearranged algebraically, and the term $\mathrm{d}\boldsymbol{u}_B/\mathrm{d}t$ is isolated in order to be integrated numerically. The first-order explicit Euler scheme is employed, since the time step used for the Lagrangian component of the model is always relatively small in cavitation calculations.

	Cavitation number	Reynolds number	p_{inj}(bar)	U_{inj} (m s^{-1})	Flow regime
Large-scale	1.05	221 700	1.775	11.14	Incipient
	1.63	253 400	2.090	12.73	Fully developed
Real-size sharp inlet	499	~16 500	500	~240	Fully developed
Real-size rounded inlet	499	~19 000	500	~280	Incipient

TABLE 2. Test cases referring to the single-hole nozzle and used for model validation.

	Cavitation number	Reynolds number	p_{inj} (bar)	U_{inj} (m s^{-1})	Flow regime
Large-scale	0.45	21 000	1.80	9.84	Non-cavitating
	1.09	30 200	2.40	14.20	Incipient
	1.48	34 100	3.00	16.00	Fully developed
Real-size	5.00	5 300	90.00	91.00	Incipient
	15.00	5 000	80.00	86.00	Fully developed

TABLE 3. Test cases referring to the six-hole nozzle with the needle at its nominal lift of 300 μm and used for model validation.

	Cavitation number	Reynolds number	p_{inj} (bar)	U_{inj} (m s^{-1})	Flow regime
Large-scale	1.48	~26 800	2.8	12.6	Incipient
	2.39	~33 200	4.0	15.6	Fully developed
Real-size	5.00	~4 100	90.0	~72.0	Incipient
	15.00	~4 000	80.0	~70.0	Fully developed

TABLE 4. Test cases referring to the six-hole nozzle with the needle at its low lift of 80 μm and used for model validation.

2.4.5. *Effect of turbulence on bubble motion*

The turbulent nature of the flow has a significant effect on bubble motion, since the fluctuating liquid velocity causes some dispersion in its movement. Due to the uncertainties regarding the applicability of complex modelling efforts to this issue, the approach of Farrell (2003) has been followed in the current model, where a Gaussian approach is employed. Typically, the effect of turbulence upon the particle's movement is modelled with the addition of a fluctuating component to the mean velocity of the liquid phase, namely $\boldsymbol{u}_L = \bar{\boldsymbol{u}}_L + \boldsymbol{u}'_L$; this velocity is used subsequently in (34), the single-bubble momentum equation, as the instantaneous continuous-phase velocity. For the calculation of the fluctuating velocity component, a Gaussian distribution is assumed, which has zero mean value and standard deviation of $\sigma = \sqrt{2k_L/3}$. The Gaussian approach used for the evaluation of the continuous-phase fluctuating-velocity component is given as

$$u'_{L,i} = \sigma^* \text{erf}^{-1}(2r_i - 1), \text{ where } \sigma^* = \min(\sqrt{4k_L/3}, 0.2\,|\boldsymbol{u}_L|), \tag{40}$$

where erf^{-1} is the inverse error-function and r_i is a random number sampled from a uniform distribution. This Gaussian function does not allow high fluctuating velocities to be calculated in areas in which the mean velocity of the liquid is low; this modification has been considered necessary from comparison of predictions against cavitation images, as reported in detail by Giannadakis (2005).
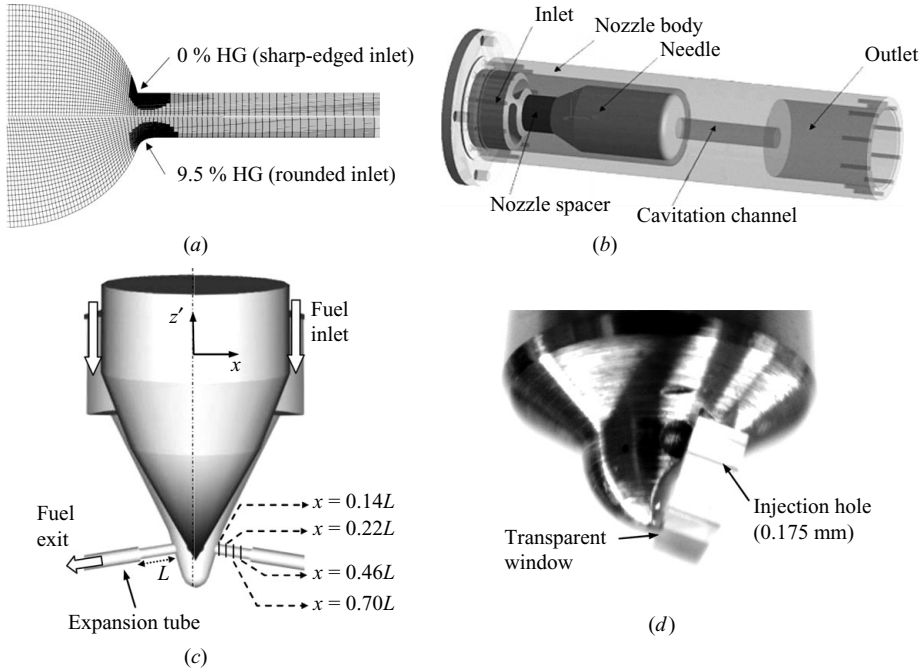
FIGURE 8. (*a*) Grid for the 0 %HG nozzle with 4590 cells and the 9.5 %HG nozzle with 4521 cells. (*b*) Large-scale single-hole nozzle used for CT measurements. (*c*) Transparent nozzle and LDV measurement planes. (*d*) Optically accessible real-size nozzle and visualization area.

3. Test cases

Numerous test cases were simulated for the experimental validation of the cavitation model. Tables 2–4 summarize the more detailed validation test cases to be presented here. Table 2 includes the real-size single-hole nozzle test cases reported in König & Blessing (2000) and Walther *et al.* (2001). This particular nozzle is the planar version of a single-hole sac-type axisymmetric nozzle used in the past by Walther *et al.* (2001) for experimental studies on cavitation. The experimental data consist of high-speed images obtained in the planar channel, where cavitation was formed in the upper section of the hole inlet. Two different geometries were tested, as shown in figure 8(*a*). The first one had a sharp hole entry (0 % degree of hydro-grinding, referred to as %HG), which promoted cavitation, while the second one had a 9.5 %HG and, thus, significantly less cavitation; the percentage indicates for each nozzle the flow rate increase relative to the sharp design due to hole inlet rounding by the hydro-grinding process. The rounding of the second nozzle was selected to be such that the two nozzles would give roughly the same flow rate at the same operating pressure, since the sharp-edged nozzle had a slightly larger hole size of 205 μm compared to the 192 μm of the hydro-ground one; the needle lift for both cases was 250 μm. Two-dimensional simulations of these geometries were performed using grids that featured local refinement at the point of cavitation incipience. Various grids were tested in order to check the model behaviour, and those finally selected were dense enough to allow grid-independent results. The working fluid was diesel with density $\rho = 835\ \mathrm{kg\,m^{-3}}$ and dynamic viscosity $\mu = 2.5 \times 10^{-3}\ \mathrm{kg\,m^{-1}\,s^{-1}}$. For both cases, the upstream pressure was provided by a common-rail system and remained relatively

constant during the injection period; its nominal value was approximately 500 bar, but for the simulations the actual transient pressure trace, measured at a location very close to the nozzle inlet, was used as boundary condition. The model inputs controlling bubble formation are (i) the initial volume fraction with respect to the available volume for nucleation and (ii) the minimum and maximum initial radii of the bubble with the corresponding weighting number densities to be used in their size *pdf* described by (12). The corresponding values used for these initial parameters were (i) $\alpha_{V0} = 0.05\,\%$ for the initial volume fraction of the nuclei and (ii) $R_{min} = 0.25\,\mu$m with $n_{min} = 10^{20}$ nuclei m^{-4} and $R_{max} = 1.5\,\mu$m with $n_{max} = 10^{19}$ nuclei m^{-4} for the size *pdf* parameters. With these values the calculated initial number density of each parcel n_{parcel} varied from 500 to 2000 bubbles per parcel. The combination of the above parameters gives an average number density estimated by the *pdf* of $N_{aver} = 2.3 \times 10^{14}$ nuclei m^{-3}; this value refers to nuclei of all possible diameters within the aforementioned limits of the considered *pdf*. In order to compare with a monodisperse distribution, had bubbles of uniform $R = 1\,\mu$m been formed, then their number density equivalent to the one estimated above would have been $N = 10^{14}$ nuclei m^{-3}, which is in agreement with values that have appeared in the literature for real-size nozzle simulations (Yuan *et al.* 2000; Yuan & Schnerr 2001).

The large-scale single-hole nozzle used for the CT images is shown in figure 8(*b*); this particular sharp-edged nozzle has been designed and manufactured for the quantitative validation of the cavitation model described earlier. Its hole diameter is 20 mm, and its hole length is 100 mm. Details about the experiments performed in this nozzle can be found in Roth (2004) and Bauer (2005); here, only sample results are included to provide evidence of model validation. The presented results refer to two different cavitation numbers of 1.05 and 1.63, respectively. Although the difference between these operating points is not significant, the actual flow regime differences observed were significant. The lower cavitation number case corresponds to the so-called incipient cavitation regime, where the cavitation structures fully collapse before reaching the hole exit. The higher cavitation number case corresponds to the 'fully developed' cavitation regime, where the cavitation structures formed at the hole inlet survive up to the hole exit. Although the transition from one regime to the other does not happen at the same cavitation numbers for the large-scale and real-size nozzle, it is a specific characteristic of the flow that can be easily identified from the CCD images and used as a criterion to assess the predictive capability of cavitation models. The working fluid for these tests was water with density $\rho = 1000$ kg m^{-3} and dynamic viscosity $\mu = 1.05 \times 10^{-3}$ kg m^{-1} s^{-1}. The initial radii for the logarithmic *pdf* were selected to be $R_{min} = 2.5\,\mu$m and $R_{max} = 50\,\mu$m. For this particular case a broader range of nucleus sizes was considered, due to the fact that this geometry was significantly larger than the rest, and the experiment was performed with water which, as already mentioned, is usually contaminated by nuclei of a broader size range. The numerical grid used consisted of $\sim 1.6 \times 10^5$ cells, with approximately 20 000 bubble parcels present inside the injection hole at every time step. As has been pointed out, although boundary conditions of constant inlet flow rate were employed, the flow itself was transient. This was mainly due to the formation, growth and transport of the cavitation bubbles, which, in turn, affected the pressure and velocity distribution inside the injection hole. This necessitated approximately 100 continuous-phase time steps of 5×10^{-4} s each in order to reach a pseudo-steady flow condition comparable to the CT measurements; the time step for the tracking of the cavitation bubbles was 2.5×10^{-6} s.

Model validation was also performed against a realistic six-hole diesel nozzle geometry; tables 3 and 4 summarize the test cases simulated with this nozzle operating at its nominal and low needle lifts, respectively. This nozzle geometry corresponds to that of a typical vertical mini-sac diesel injector; the nominal hole diameter of the real-size nozzle is 0.175 mm which corresponds to 3.5 mm for the model enlarged 20 times. The holes are equally distributed every 60° around the periphery, while their inclination angle is 11° from the horizontal. The nominal needle lift is 0.3 mm which corresponds to 6.0 mm in the enlarged model; the investigated value of lower needle lift corresponds to 0.08 mm in the real-size injector and 1.6 mm in the enlarged model. Detailed experimental investigations about this nozzle have been reported in past papers (Afzal *et al.* 1999; Arcoumanis *et al.* 2000; Roth *et al.* 2002). They include high-speed/CCD flow images and LDV measurements obtained in the large-scale fully transparent nozzle, shown in figure 8(*c*), and CCD flow images from the real-size nozzle incorporating a transparent window allowing for optical access in one of the six holes, shown in figure 8(*d*). Calculated results to be presented here include both the time-averaged mean velocity component in the direction of the injection hole as well as its standard deviation with respect to the temporal mean; the latter is due to the cavitation-induced unsteadiness of the flow. For both nozzles, various cavitation numbers have been selected for presentation. For the large-scale six-hole nozzle at its nominal lift, in addition to the measurements for the cavitating conditions, LDV measurements corresponding to the lowest cavitation number for this nozzle/lift combination ($CN = 0.45$) are presented for non-cavitating conditions as well. For all the other cavitation numbers reported, the lower one corresponds to the 'incipient cavitation regime', and the higher cavitation number corresponds to 'fully developed cavitation'. Regarding the initial values of the cavitation sub-models, the same physical properties and assumptions as those described earlier for the real-size single-hole nozzles have been also used here, with the exception of the initial radii of the logarithmic *pdf* for the large-scale nozzle; in agreement with experimentally observed scaling of nucleus sizes, the selected values were $R_{min} = 1\,\mu$m and $R_{max} = 15\,\mu$m. Moreover, in the experiments with the large-scale nozzle a mixture of 32 % by volume of tetraline (1,2,3,4-Tetrahydronaphthalene) and 68 % by volume of oil of turpentine was taken as the working fluid in order to produce a liquid that has the same refractive index as the acrylic nozzle and has fuel properties similar to diesel (density and kinematic viscosity of 893 kg m^{-3} and 1.64×10^{-6} m^2 s^{-1} at 25 °C, respectively). This refractive-index-matching method (Arcoumanis, Nouri & Andrews 1992) enables optical access without any distortion of light at the liquid–solid interfaces, allowing imaging techniques and laser Doppler velocimetry to be applied successfully.

4. Results and discussion

In this section the various results obtained with the developed model are presented. Initially the results from the single-hole nozzle studies are presented, followed by validation studies from the more practically relevant six-hole nozzle geometry.

4.1. *Single-hole nozzle*

The first nozzle series simulated is the transparent real-size single-hole one. Due to the symmetrical design, half-nozzle simulations in a two-dimensional plane have been performed. Figure 9 shows a comparison between model predictions against CCD
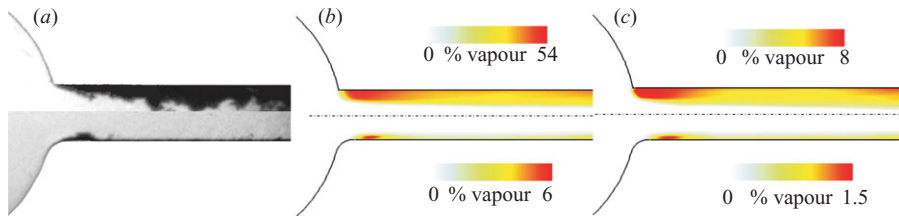
FIGURE 9. (*a*) CCD images of temporal cavitation vapour distribution from König & Blessing (2000) for the 0%HG (top) and 9.5%HG nozzle (bottom). (*b*) Temporal mean cavitation volume percentage distribution. (*c*) Standard deviation of cavitation volume percentage ($p_{inj} = 500$ bar, $p_{back} = 1$ bar).

images of cavitation inside the sharp-edged and rounded inlet nozzles. Although the instantaneous CCD images of figure 9(*a*) reveal the extent of cavitation inside the flow channel, they do not provide any quantitative information about the flow, contrary to predictions which characterize the temporal mean vapour volume fraction distribution over the whole injection event. Figure 9(*b*) shows the predicted effect of hole inlet rounding on the mean cavitation volume fraction. Large differences do exist between the two nozzles, with more than 50% of the hole covered by cavitation in the sharp-inlet nozzle, while the corresponding prediction for the rounded nozzle is just ∼6%, with the cavitation zone significantly reduced. Clearly, the geometric characteristics of the hole entry have a dominant effect on the amount of vapour volume formed as well as on its growth. Moreover, both predictions and flow images show that cavitation is rather unstable even during the main injection period despite the fact that the needle is fixed at its maximum lift, and the injection pressure provided by the common-rail injection system does not change considerably. This can be realized in figure 9(*c*) which shows the predicted standard deviation of the mean cavitation vapour volume fraction, attributed to the nucleation process taking place at the inlet to the injection hole in areas in which the local pressure falls below the vapour pressure of the liquid. Once vapour is produced, the simulated pressure at this location 'recovers' towards the threshold value or even exceeds it and results in no new vapour volume formation. This, in turn, induces new tension (local pressure below vapour) in the computational cells that become re-occupied with liquid, and the process continues in a cyclic pattern.

It is evident from the above discussion that model predictions are sensitive to the amount of vapour produced, and thus quantitative validation is required. Such measurements of the vapour volume fraction produced in cavitating flows have been reported in Roth (2004) and Bauer (2005) for the large-scale single-hole nozzle and are used here for model validation. The conditions to be reported refer to two different cavitation numbers corresponding to the incipient and fully developed cavitation regimes. Past studies have revealed that the cavitation number is the dominant flow parameter that determines the flow regime inside cylindrical nozzle holes instead of the Reynolds number. This can also be seen in figures 10 and 11, where experiments and model predictions are presented for the low and high *CN* cases, respectively. For the low *CN* case the CCD images, a sample of which is plotted in figure 10(*a*), show that cavitation is formed at the hole inlet and collapses within a short distance downstream into the hole. The sequence of events captured with a high-speed camera actually shows that the cavitation structures are rather unstable, something also
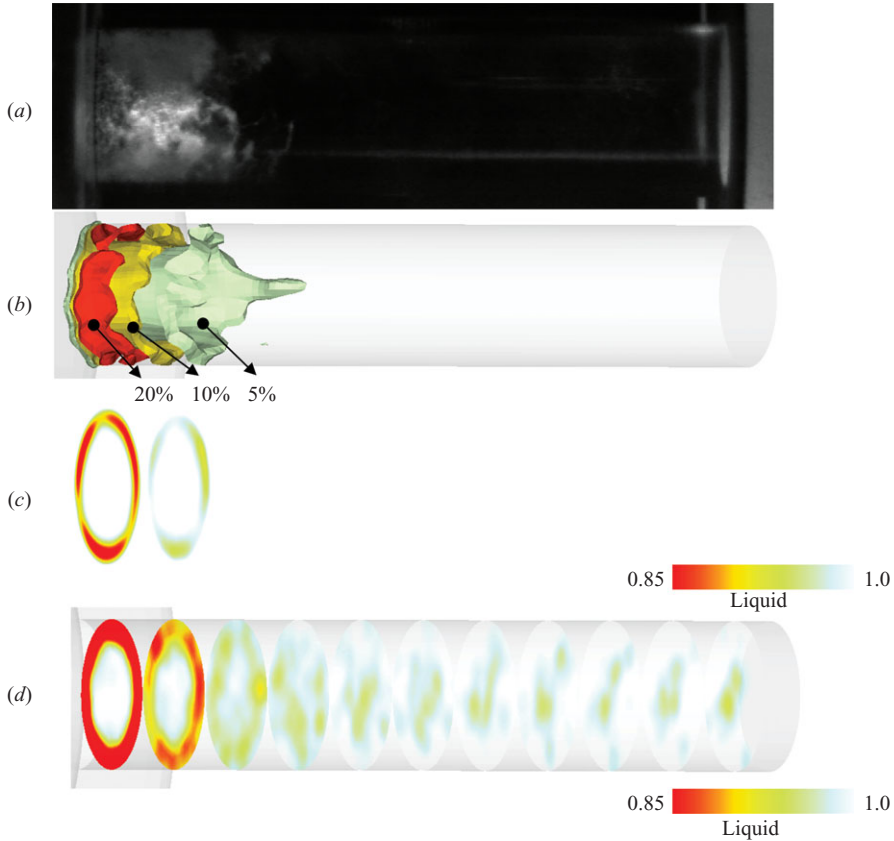
FIGURE 10. (*a*) CCD image of cavitation inside the large-scale single-hole nozzle for the incipient cavitation case. (*b*) Predicted instantaneous vapour volume fraction iso-surfaces. (*c*) CT measurements of liquid volume fraction at different cross-sections across the hole length. (*d*) Predicted liquid volume fraction.

predicted by the computational model. Figure 10(*b*) shows an instantaneous image of the predicted vapour volume fraction iso-surfaces; the model also predicts the collapse of the cavitation cloud at a distance similar to the collapse observed from the CCD images. Time-averaged liquid volume fraction measurements and predictions at cross-sections along the injection hole are plotted in figure 10(*c*, *d*), respectively. The observed differences between model predictions and experimental values are not negligible, but it is important to note that the model appears to follow quantitatively the measured cavitation trends, especially when considering that a very small change to the cavitation number may result in a fully developed cavitation regime, as shown in figure 11(*a*) in which the cavitation cloud is extended up to the hole exit. Near the inlet, and almost up to 40 % into the hole length, the amount of vapour formed seems to behave in a rather stable fashion, remaining attached to the nozzle wall surface. Breakdown of the formed vapour is observed at distances greater than 40 % of the hole length. This breakdown is associated with formation of a bubbly, rather unstable, cloud, as high-speed images have revealed. This can be also deduced from figure 11(*b*) which shows the CT measurements of the time-averaged liquid volume distribution at various cross-sections along the hole length. Close to the hole entrance, the formed vapour stays attached to the wall, and a relatively sharp interface between
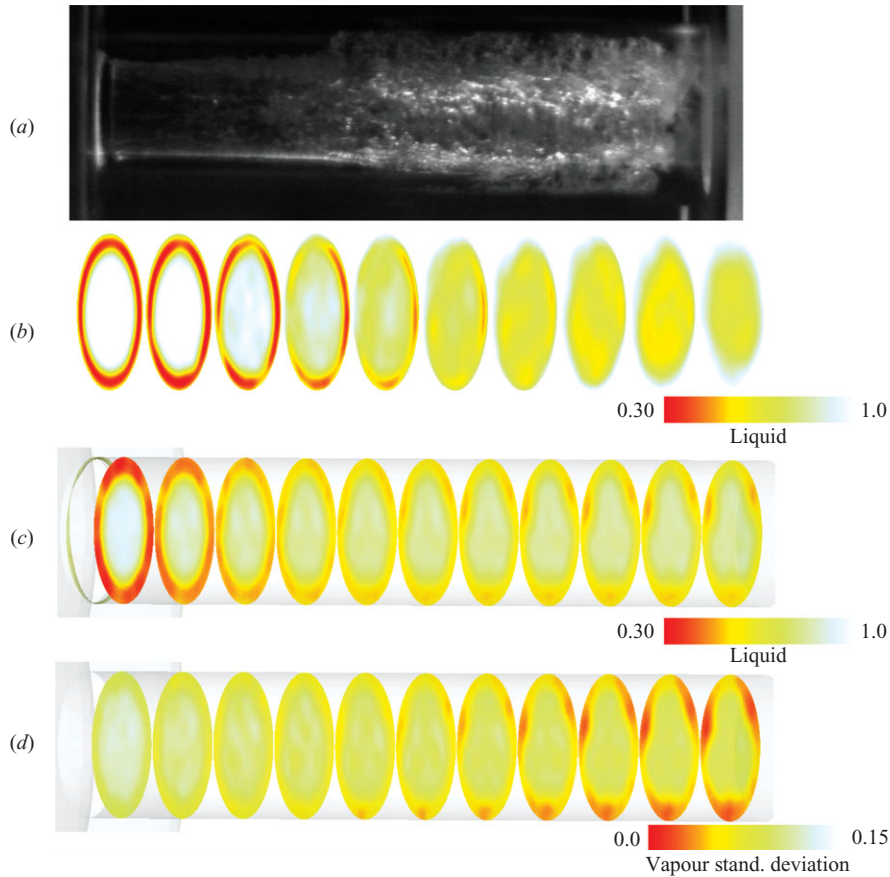
FIGURE 11. (*a*) CCD image of cavitation inside the large-scale single-hole nozzle for the fully developed cavitation case. (*b*) CT measurements of liquid volume fraction at different cross-sections across the hole length. (*c*) Predicted liquid volume fraction. (*d*) Predicted vapour volume fraction standard deviation.

the two phases is observed. Once this interface breaks down, vapour is gradually dispersed across the whole cross-section of the discharge hole, in agreement with the model predictions presented in figure 11(*c*). Estimates of the spatial distribution of the liquid volume fraction standard deviation along the same cross-sections are plotted in figure 11(*d*); these model predictions indicate that, close to the hole inlet, the standard deviation of the vapour is almost zero, while maximum values are observed towards the hole exit. This is an important result, since it demonstrates that the model not only captures the time-averaged cavitation volume fraction levels but also indicates the locations at which cavitation becomes unstable. Predictions reported recently in Gavaises *et al.* (2007) have indicated that this predictive capability of the model allows the link to cavitation erosion, observed within the injection hole of high-pressure fuel injection systems, to be identified. Figure 12 depicts quantitative comparison between model predictions and CT measurements of the liquid volume fraction, averaged over all the cross-sections along the hole length, for both test cases simulated. In both cases, the model predicts with reasonable accuracy the amount of vapour produced close to the hole entry as well as the transition from one flow regime to the other.
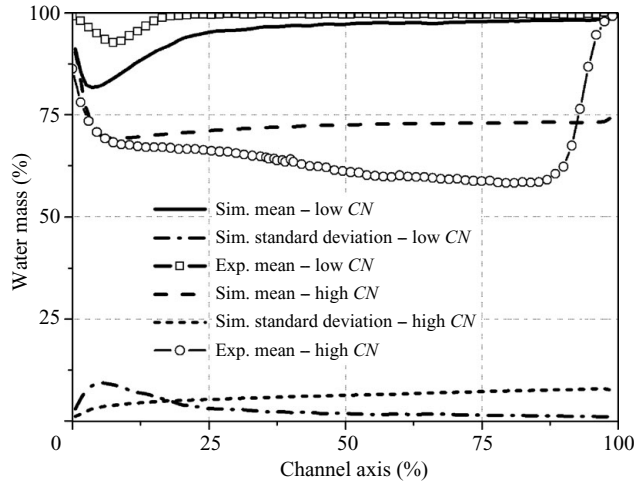
FIGURE 12. Comparison between experimental data and model predictions for the spatially averaged liquid volume percentage across cross-sections along the injection hole for the two cavitation numbers investigated.

More discrepancies are realized towards the hole exit for the higher CN case; up to 90 % of the hole length the CT measurements indicate that the amount of vapour actually increases, while predictions indicate an almost fixed percentage of vapour. Moreover, from that point onwards and up to the hole exit the CT measurements show a sharp increase in water mass, whereas in the simulation there is only a slight decrease in the amount of vapour at the very end of the hole. Possible reasons for the observed differences include the non-resolved fluctuations of the local pressure that can result in further growth or collapse and the internal bubble re-initialization pressure required upon bubble breakup. Due to the significantly smaller pressure differences encountered in cavitating flows in large-scale nozzles, the temporal resolution of pressure fluctuations in the simulation of such cases is more critical than for cavitating flow simulations in real-size nozzles; this fact points to the need for a turbulence model that is less momentum-dissipative than the typical two-equation models, like the standard k-ε adopted here. Regarding the already-discussed issue of the internal bubble pressure, the present model assumes that when a bubble breaks, the contaminant gas partial pressure is re-initialized based on the local liquid pressure under equilibrium conditions. In this way, the bubbles' 'memory' of being compressed at much higher pressures before entering the hole, responsibile for a growth production and subsequent collapse according to the R-P equation, is lost. Since bubble breakup is observed at the mid-distance of the injection hole at which the local pressure is almost equal to the back pressure, it is expected that the above assumption causes the bubbles to become less responsive to the very small local pressure variation they encounter from that point to the hole exit. Unfortunately, in the absence of a rigorous theory for the calculation of the internal bubble pressure during breakup, the adopted simplification may give rise to the observed differences between the predicted and measured values.

From this part of the investigation on single-hole nozzles, it has become evident that the model is capable of predicting some important aspects of cavitating flows in injector nozzle holes. These include the inherent instability of cavitation development even at fixed operating conditions, the transition between the incipient and the
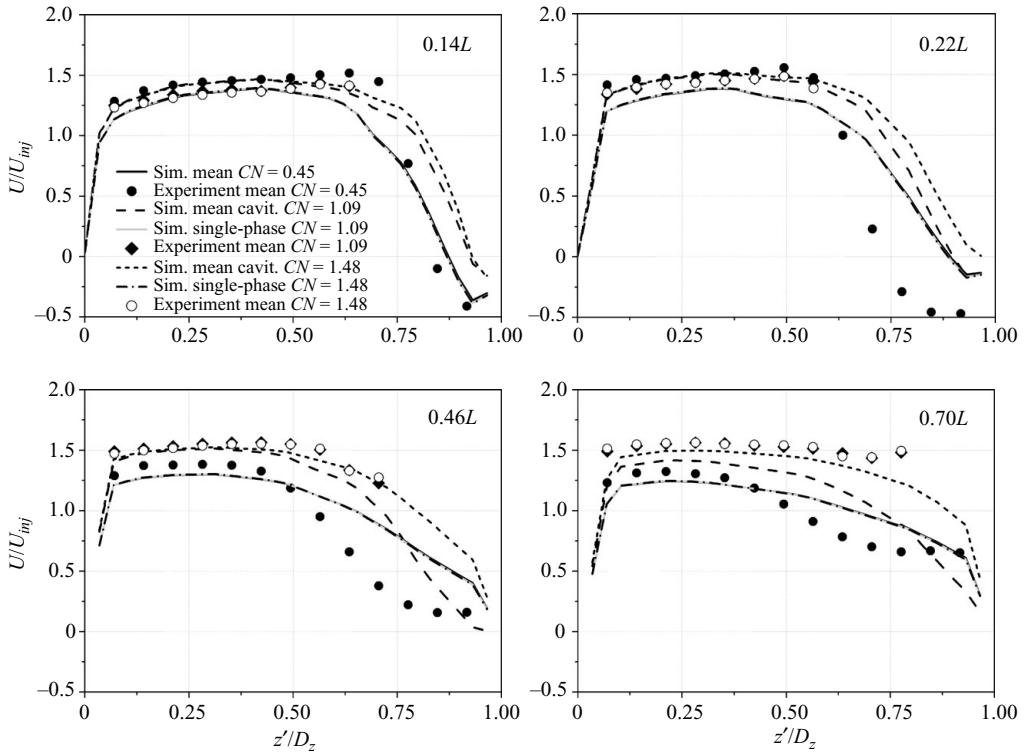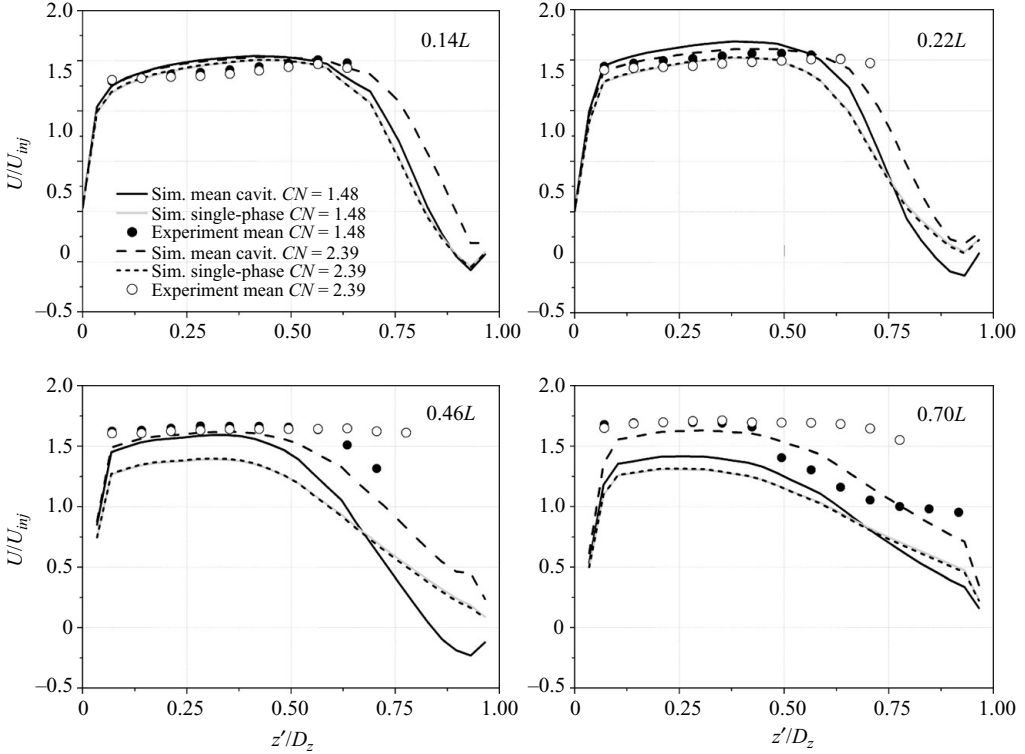
FIGURE 13. Comparison between computational and experimental results for the mean axial velocity at four different locations inside the injection hole for all conditions investigated (nominal needle lift).

fully developed cavitation regime as well as the amount of vapour produced. The applicability of the model to more realistic six-hole diesel nozzle geometries is explored next.

4.2. *Multi-hole nozzle*

As has been pointed out, in the enlarged six-hole injector both CCD images and LDV measurements are available from Roth (2004). In particular, mean and r.m.s. velocity measurements in the direction of the injection hole have been obtained at different vertical planes, shown in figure 8(c). Results are presented here for two different cavitation numbers corresponding to two different cavitation regimes and two needle lifts. Further results include, for the nominal lift case of the enlarged nozzle, LDV measurements and predictions for non-cavitating conditions. Figure 13 shows the comparison of the mean velocity for all cavitation numbers investigated at the nominal needle lift of 6 mm (equivalent to 0.3 mm in the real size), while figure 14 shows the corresponding results for the lower needle lift case of 1.6 mm. The velocity values plotted have been normalized by the mean injection velocity derived from the flow rate and the hole cross-sectional area. In addition to the time-averaged cavitating predictions, single-phase simulation results for the cavitating cases are also presented. This allows the effect of increasing cavitation number to be realized and, moreover, the acceleration of the fuel due to cavitation to be appreciated more clearly when compared to the single-phase case. Beginning with the non-cavitating conditions ($CN = 0.45$) for the nominal lift case, it can be argued that the relative agreement

FIGURE 14. Comparison between computational and experimental results for the mean axial velocity at four different locations inside the injection hole for all conditions investigated (low needle lift).

between the predictions and the measurements is quite satisfactory. Nevertheless, there is some discrepancy in the shape of the velocity profile at locations near the upper part of the hole, where the experiment shows some decay of the axial velocity at the locations just before the middle of the hole length ($x = 0.22L$ and $x = 0.46L$). Possible explanations for the observed difference include that, in multi-hole nozzles, the flow can never be truly symmetric amongst the holes due to some unavoidable needle eccentricity; this alone could explain the velocity differences in the middle plane. However, as will be seen from the r.m.s. comparisons, another reason could be that a more sophisticated turbulence modelling approach is needed, with which potentially present anisotropic and non-equilibrium effects would be captured. In any case, the difference between the non-cavitating velocity measurements and their corresponding predictions determines the uncertainty level for the velocity comparisons in the cavitating cases. As can be seen in figures 13 and 14, in the axial location close to the hole inlet ($x = 0.14L$), the model predicts a velocity profile similar to the measured one. However, moving further downstream inside the injection hole, the model seems to 'underpredict' the velocity level close to the hole exit ($x = 0.70L$) for the incipient cavitation case, but it seems to match closely the measured higher velocities for the two fully developed cavitation cases. Towards the mid-plane ($x = 0.46L$) and at the hole exit ($x = 0.70L$), the predictions are close to the experimental values. On these locations, the differences between the non-cavitating and the fully cavitating cases are maximized. As can be seen, cavitation leads to an acceleration of the flow of ~15%
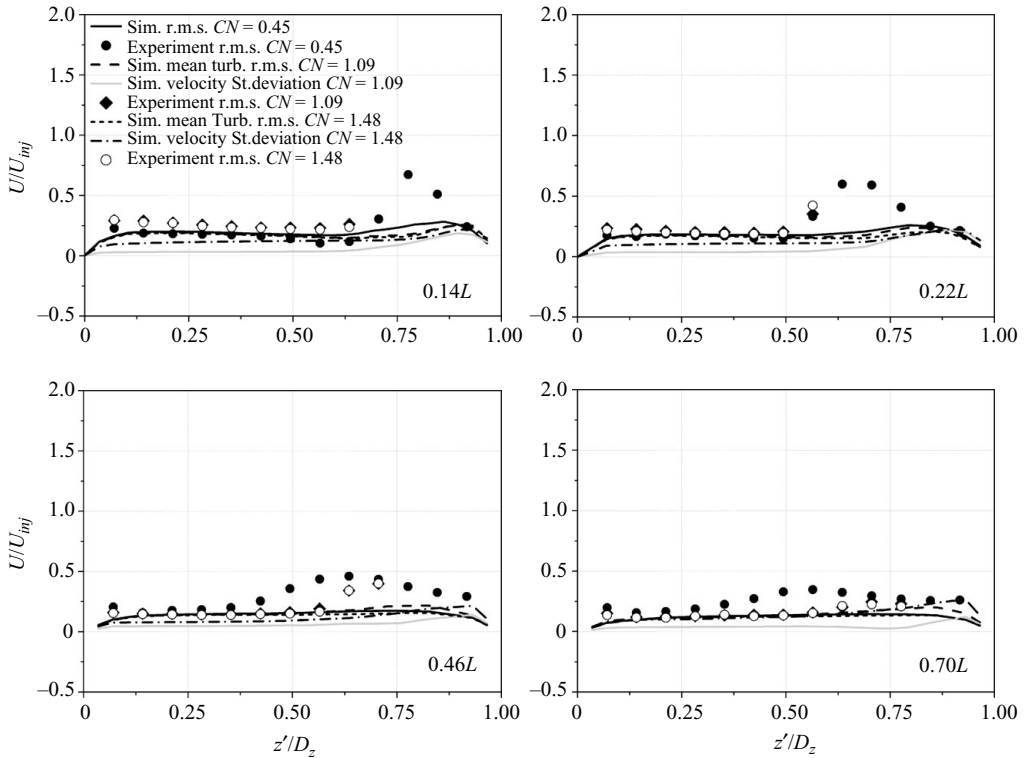
FIGURE 15. Comparison between computational and experimental results for the turbulent (r.m.s.) velocity at four different locations inside the injection hole for all conditions investigated (nominal needle lift).

for this particular nozzle and operating conditions; this acceleration is higher for the lower needle lift case in which more cavitation is formed due to the sharper turn of the flow imposed by the restricted needle seat flow passage. As mentioned already, the corresponding measurements and predictions for the r.m.s. (turbulent) velocity component at the same locations and for the same operating conditions are presented in figures 15 and 16, respectively. From the comparison of the r.m.s. velocities for the non-cavitating condition in figure 15, it can be seen that for all locations there is a peak in the measured r.m.s. velocity which is not captured by the predictions. This peak occurs at nearly 75 % of the hole height, and it seems to settle down downstream and relocate towards the centre of the hole height. This discrepancy may justify the need to explore a more sophisticated approach to turbulence modelling in the future, as already mentioned. Regarding the cavitating cases, in both graphs two different r.m.s. velocities are calculated; the first one is the time-averaged r.m.s. velocity estimated from the turbulence model, while the second one is the velocity temporal standard deviation from the mean value at each location. Unfortunately, this information could not be resolved from the LDV measurements in which the unsteadiness that is recorded includes the contribution of both turbulence and the mean velocity temporal variation due to the fluctuating nature of cavitation. As is clear from the plotted results, the standard deviation velocity seems to have relatively smaller values at the lower section of the hole in which mainly liquid flow is present but increases substantially in the cavitating region. The r.m.s. velocity calculated from
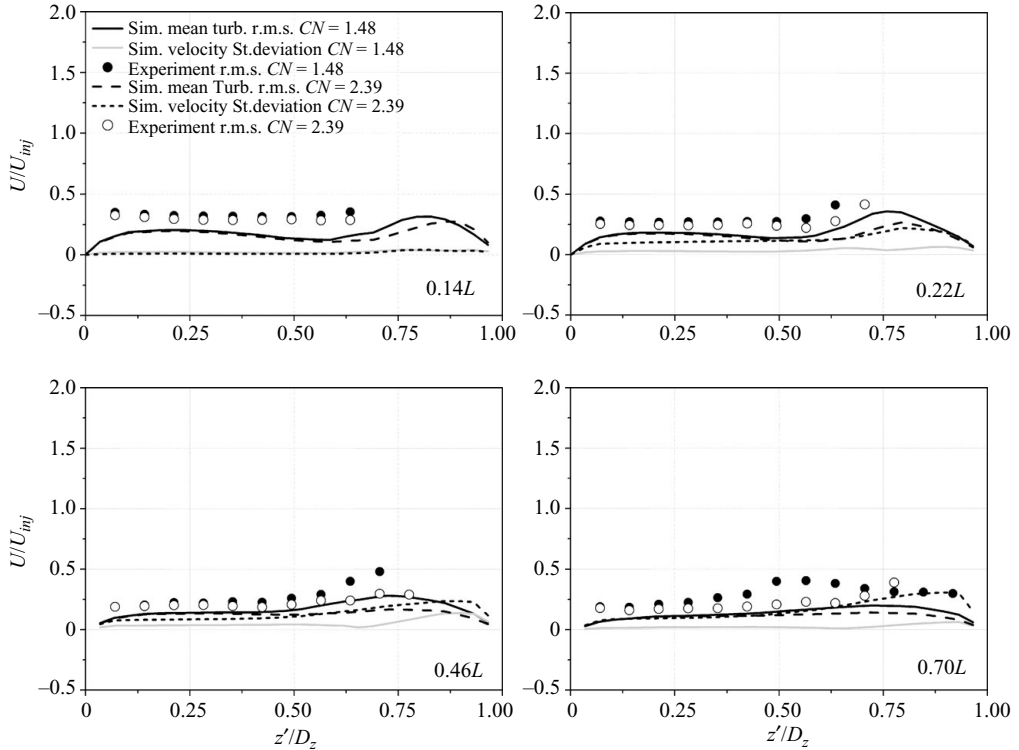
FIGURE 16. Comparison between computational and experimental results for the turbulent (r.m.s.) velocity at four different locations inside the injection hole for all conditions investigated (low needle lift).

the turbulence model seems to be quite close to the measured values at the lower part of the hole; this seems to be captured well by the model. Moving towards the cavitating region, the measured r.m.s. values increase substantially up to the point at which measurements could not be obtained, due to the very dense vapour cloud present. This trend is captured in the model, although actual values deviate in some locations from the measured ones. It is also interesting to note that the fluctuating part of the mean velocity may take values as high as those calculated from the turbulence model itself. Arguably, cavitation appears to induce an additional unsteadiness in the flow, apart from that of turbulence, and this combined instability is expected to have a positive effect on liquid-core atomization.

The last of the validation studies to be presented here is qualitative rather than quantitative; it shows a comparison of the cavitation structure inside the injection hole as visualized using a CCD camera, against model predictions. Results for the large-scale nozzle are presented in figures 17 and 18 for the nominal needle lift case as seen from the side view and the top view, respectively. Results are presented for both the incipient and the fully developed cavitation number cases. The corresponding flow images and model predictions for the low needle lift case are shown in figures 19 and 20 from the same side and top views, respectively. Finally, flow images obtained inside the transparent hole window of the real-size nozzle can be seen in figures 21 and 22 for the two equivalent needle lifts, respectively. For the large-scale nozzle, the CCD images show quite an unsteady flow development for both *CN* cases. For
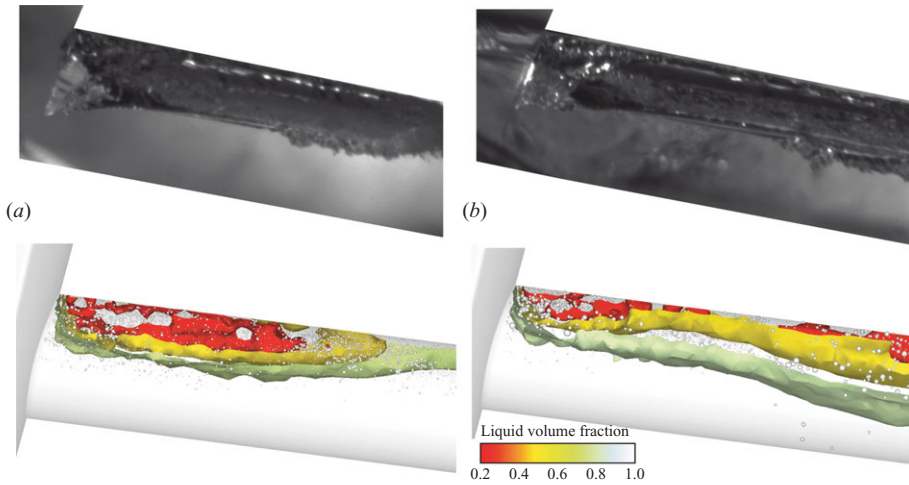
FIGURE 17. Side-view comparison between CCD images and model predictions for the vapour distribution on the surface of the large-scale nozzle: (*a*) incipient cavitation number case ($CN = 1.09$) and (*b*) fully developed cavitation ($CN = 1.48$) at nominal needle lift.
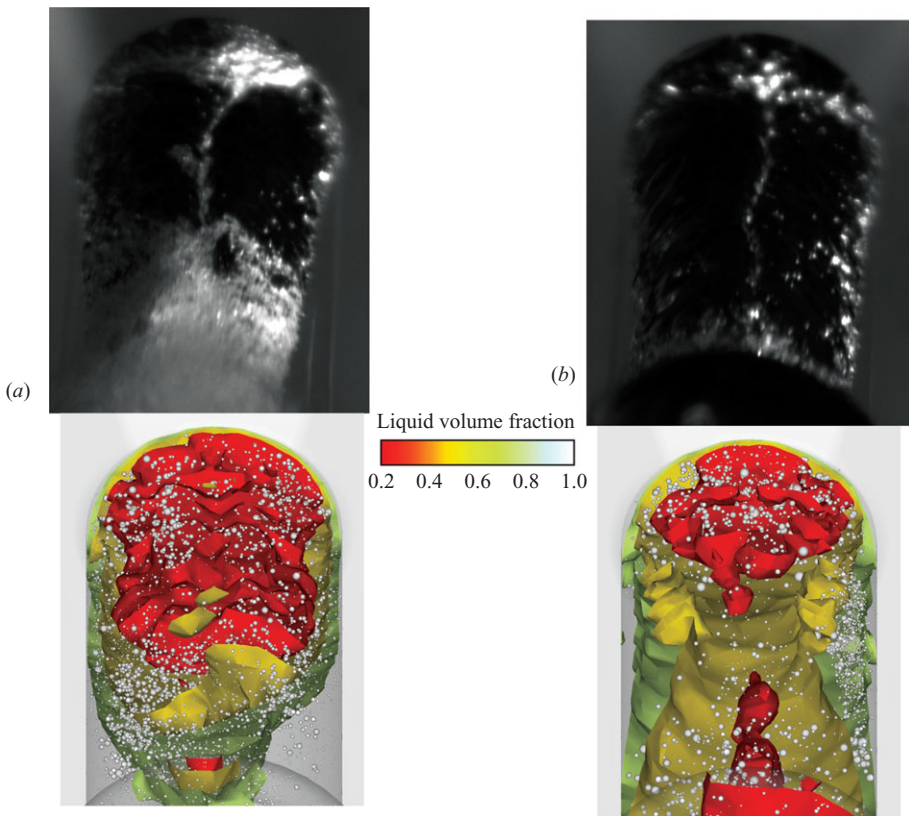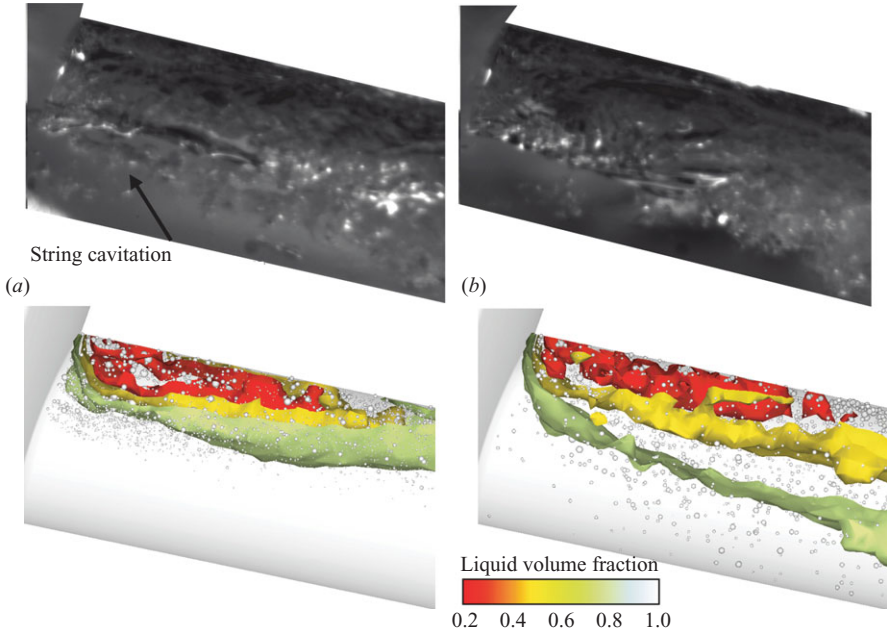

FIGURE 18. Top-view comparison between CCD images and model predictions for the vapour distribution on the surface of the large-scale nozzle: (*a*) incipient cavitation number case ($CN = 1.09$) and (*b*) fully developed cavitation ($CN = 1.48$) at nominal needle lift.

FIGURE 19. Side-view comparison between CCD images and model predictions for the vapour distribution on the surface of the large-scale nozzle: (*a*) incipient cavitation number case ($CN = 1.48$) and (*b*) fully developed cavitation ($CN = 2.39$) at low needle lift.
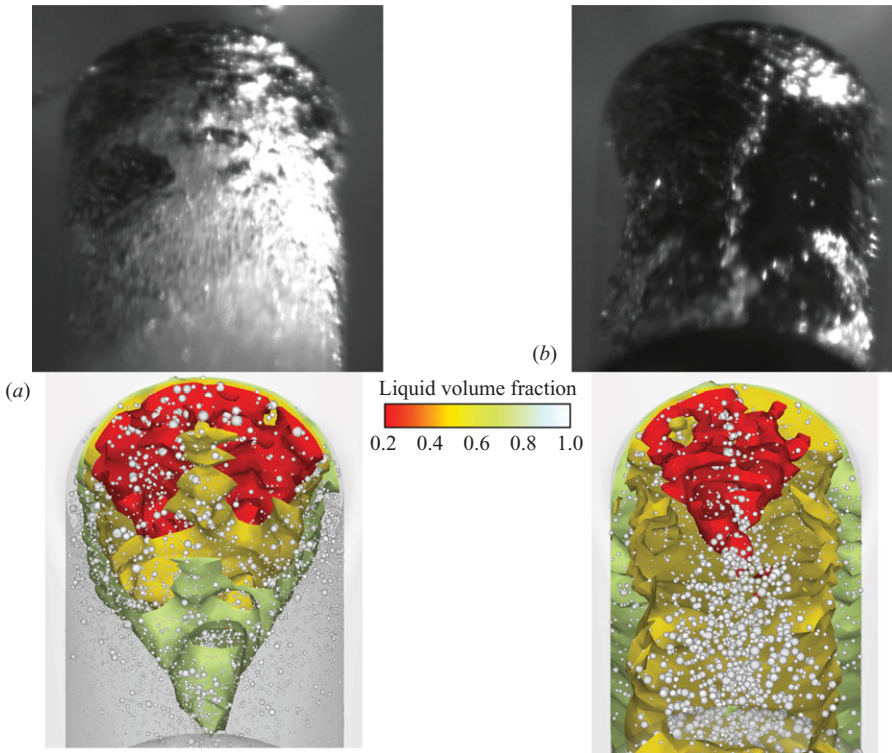

FIGURE 20. Top-view comparison between CCD images and model predictions for the vapour distribution on the surface of the large-scale nozzle: (*a*) incipient cavitation number case ($CN = 1.48$) and (*b*) fully developed cavitation ($CN = 2.39$) at low needle lift.
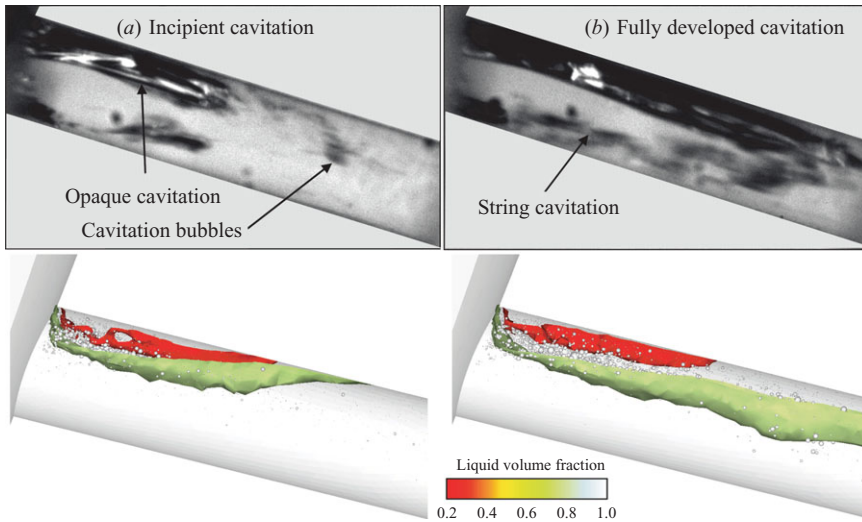
FIGURE 21. Comparison between CCD images and model predictions for the vapour distribution inside the real-size nozzle: (*a*) incipient cavitation number case ($CN = 5$) and (*b*) fully developed cavitation ($CN = 15$) at nominal needle lift.
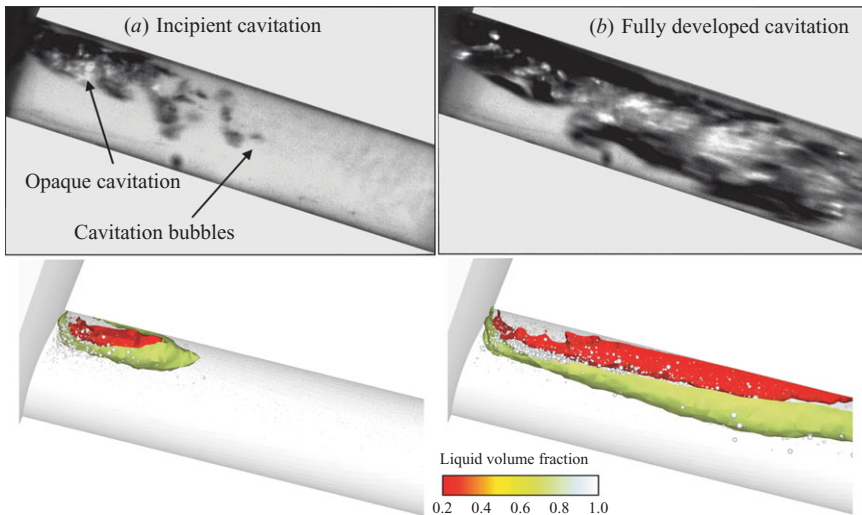

FIGURE 22. Comparison between CCD images and model predictions for the vapour distribution inside the real-size nozzle: (*a*) incipient cavitation number case ($CN = 5$) and (*b*) fully developed cavitation ($CN = 15$) at low needle lift.

the incipient cavitation, the bubble cloud reaches the hole exit periodically, while in the higher CN case, the bubble cloud is more opaque with a higher percentage of the hole occupied by vapour. The Eulerian–Lagrangian model predicts a similar vapour distribution; in the images plotted, three different levels of vapour volume fraction iso-surfaces are presented together with sample cavitation bubbles. The model predicts a gradual distribution of the vapour fraction with the highest values present at the top corner of the injection hole. A distinctive difference between the incipient

and developed cavitation regimes for both needle lifts can be seen in the shape of the simulated cavitation structures; from the side-view comparison shown in figures 17 and 19 one can note that in the incipient cavitation cases vapour structures are relatively more confined. The cavitation pockets appear to vanish towards the exit of the hole, and moreover, the plotted liquid volume fraction iso-surfaces are relatively close; this means that vapour volume fraction gradients are large, indicative of a sharp vapour-to-liquid transition. In contrast, for the developed cavitation cases cavitation structures appear to spread towards the exit of the hole; moreover, the distance between the plotted liquid volume fraction iso-surfaces appears to become larger as well. The latter means that a relatively homogeneous bubble cloud is formed towards the exit of the hole. Similar differences between the two cavitating regimes can be identified in the top-view comparison shown in figures 18 and 20, where the variation in the extent of the cavitation structures is also evident. Once again, in the incipient cases cavitation appears to diminish around the hole exit, whereas for the fully developed cavitation cases vapour structures appear to exit the hole with almost the same extent.

A similar situation is also found when comparing CCD images and model predictions for the real-size nozzle. The model seems to capture not only the change of the flow with respect to the increased cavitation number but also the relative increase observed with decreasing needle lift; this is caused by the more sudden flow turn experienced by the liquid just upstream of the hole entry at decreasing needle lifts. From the comparison with the large-scale nozzle experimental data it can be argued that, similar to the single-hole nozzle, the cavitation model captures both qualitatively and quantitatively the observed flow regimes, the mean and r.m.s. velocities as well as the change of the flow regime with respect to cavitation number and needle lift. Concerning the qualitative agreement between the experiment and the simulations it is quite satisfactory even in the case of the realistic six-hole nozzle geometry. Moreover, it seems that it is easier for predictions of the real-size nozzle to match the experimental images, possibly due to the shorter residence time available to the cavitation bubbles inside the injection hole. This may prevent uncertainties inherent in the rather incomplete physical sub-models from becoming relatively important.

5. Conclusions

The predictive capability of a stochastic Lagrangian multi-dimensional CFD model accounting for the onset and development of cavitation inside diesel nozzle holes has been assessed against experimental data. The fluid flow conservation equations have been solved numerically on fully unstructured numerical grids, which allows modelling of complex nozzle geometries and the cavitating phase. A numerical method able to simulate flow cases in which the size of the formed bubble parcels exceeds that of the underlying numerical cells has been developed. The model accounts for a number of physical processes considered to be taking place in cavitating nozzle flows. Cavitation is triggered by pre-existing nuclei assumed to be present inside the bulk of the liquid and consisting of a mixture of compressed dissolved gas and vapour. Once they reach areas in which the local pressure falls below the threshold pressure for cavitation, bubble growth/collapse is simulated using the full form of the R-P equation. Further phenomena such as bubble breakup, coalescence and turbulent dispersion have been considered for the first time in cavitation flow models and found to play a major role in model predictions. Model validation has been performed

against numerous experimental data for real-size and large-scale models of single and multi-hole nozzles. For the single-hole nozzle, high-speed cavitation imaging under injection pressures up to 500 bar in nozzles having different degrees of hydro-grinding at the hole inlet has been compared against model predictions, while CT measurements of the liquid volume fraction obtained in a sharp-edged large-scale single-hole nozzle, designed solely for the validation of the current cavitation model, have been used for quantitative evaluation of the amount of cavitation vapour produced and distributed inside the nozzle hole. High-speed CCD images obtained inside a real-size six-hole mini-sac nozzle, modified to incorporate a transparent hole window, have further been used for model validation. In addition to CCD images, LDV measurements of the liquid mean and r.m.s. velocities inside an identical large-scale fully transparent nozzle model have been used for further quantitative validation. Results available for two different cavitation numbers and two needle lifts, which correspond to different cavitation regimes formed inside the injection hole, have been included. Comparison between model predictions and experimental data has revealed that the developed model captures the increase of the mean liquid velocity caused by the onset and development of cavitation. The same is also true in the case of the r.m.s. velocity which has been found to be equally influenced by the turbulent nature of the flow and by the inherent unsteadiness caused by cavitation. In conclusion, it can be argued that cavitation modelling has reached a stage of maturity at which it can consistently identify many of the effects of nozzle design on cavitation, thus making a significant contribution to nozzle performance and optimization.

REFERENCES

AFZAL, H., ARCOUMANIS, C., GAVAISES, M. & KAMPANIS, N. 1999 Internal flow in diesel injector nozzles: modelling and experiments. *IMechE Paper* S492/S2/99.

AHMADI, M. & SELLENS, R. W. 1993 A simplified maximum-entropy-based drop size distribution. *Atom. Sprays* **3**, 291–310.

ALAJBEGOVIC, A. 1999 Three-dimensional cavitation calculations in nozzles. In *Proc. Second Annu. Meeting Inst. Multifluid Sci. Technol., Santa Barbara, CA* (ed. T. G. Theofanus), pp. III. 97–III.103. Center of Risk Studies and Safety, University of California, Santa Barbara.

ALAJBEGOVIC, A., GROGGER, H. A. & PHILIPP, H. 1999a Calculation of cavitation in nozzles using the two-fluid model. In *Proc. 7th Annu. Conf. Comp. Fluid Dyn. Soc. Canada, Halifax, NS, Canada* (ed. J. Militzer), pp. 7.3–7.8. CFD Society of Canada.

ALAJBEGOVIC, A., GROGGER, H. A. & PHILIPP, H. 1999b Calculation of transient cavitation in nozzle using the two-fluid model. In *Proc. 12th Annu. Conf. Liquid Atom. Spray Systems, Indianapolis, IN*.

ANDREWS, M. J. & O'ROURKE, P. J. 1996 The multiphase particle-in-cell (MP-PIC) method for dense particulate flows. *Intl J. Multiphase Flow* **22**, 379–402.

APFEL, R. E. 1970 The role of impurities in cavitation-threshold determination. *J. Acoust. Soc. Am.* **48**, 1179–1186.

ARCOUMANIS, C., BADAMI, M., FLORA, H. & GAVAISES, M. 2000 Cavitation in real-size multi-hole diesel injector nozzles. *SAE Trans. J. Engines* **109–3**, 1485–1500.

ARCOUMANIS, C., FLORA, H., GAVAISES, M. & KAMPANIS, N. 1999 Investigation of cavitation in a vertical multi-hole injector. *SAE Paper* 1999-01-0524.

Arcoumanis, C., Gavaises, M., Nouri, J. M., Abdul-Wahab, E. & Horrocks, R. W. 1998 Analysis of the flow in the nozzle of a vertical multi hole diesel engine injector. *SAE Trans. J. Engines* **107–3**, 1245–1259.

Arcoumanis, C., Nouri, J. M. & Andrews, R. J. 1992 Application of refractive index matching to a diesel nozzle internal flow. In *Proc. Sixth Intl Symp. Appl. Laser Techniques Fluid Mech., Lisbon, Spain* (ed. R. J. Adrian *et al.*), pp. 10.4.1–10.4.7. Springer.

Arndt, R. E. A. & Maines, B. H. 2000 Nucleation and bubble dynamics in vortical flows. *J. Fluids Engng: Trans. ASME* **122**, 488–493.

Atchley, A. A. & Prosperetti, A. 1989 The crevice model of bubble nucleation. *J. Acoust. Soc. Am.* **86**, 1065–1084.

Avva, R. K., Singhal, A. & Gibson, D. H. 1995 An enthalpy based model of cavitation. In *Cavitation and Multiphase Flow Forum* (ed. J. Katz & Y. Matsumoto), ASME FED, pp. 63–70.

Badock, C., Wirth, R., Fath, A. & Leipertz, A. 1999 Investigation of cavitation in real size diesel injection nozzles. *Intl J. Heat Fluid Flow* **20**, 538–544.

Badock, C., Wirth, R. & Tropea, C. 1999 The Influence of hydro grinding on cavitation inside a diesel injection nozzle and primary breakup under unsteady pressure conditions. In *Proc. ILASS-EUROPE, Toulouse, France* (ed. G. Lavergne).

Batchelor, G. K. 1953 *The Theory of Homogeneous Turbulence*. Cambridge University Press.

Bauer, D. 2005 Planung und Durchführung von Experimenten zur Validierung eines CFD-Codes für Kavitationsströmungen. Diplomarbeit. Technische Universität Bergakademie Freiberg, Germany.

Bergwerk, W. 1959 Flow pattern in diesel nozzle spray holes. *Proc. Inst. Mech. Engrs* **173**, 655–660.

Blessing, M., König, G., Krüger, C., Michels, U. & Schwarz, V. 2003 Analysis of flow and cavitation phenomena in diesel injection nozzles and its effect on spray and mixture formation. *SAE Paper* 2003-01-1358.

Brennen, C. E. 1995 *Cavitation and Bubble Dynamics*. Oxford University Press.

Briggs, L. J. 1950 Limiting negative pressure of water. *J. Appl. Phys.* **21**, 721–722.

Bunnell, R. A. & Heister, S. D. 2000 Three-dimensional unsteady simulation of cavitating flows in injector passages. *J. Fluids Engng: Trans. ASME* **122**, 791–797.

Bunnell, R. A., Heister, S. D., Yen, C. & Collicott, S. H. 1999 Cavitating injector flows: validation of numerical models and simulations of pressure atomizers. *Atom. Sprays* **9**, 445–465.

Chaves, H., Knapp, M., Kubitzek, A. & Obermeier, F. 1995 Experimental study of cavitation in the nozzle hole of diesel injectors using transparent nozzles. *SAE Paper* 950290.

Chen, Y. L. & Heister, S. D. 1996a Modeling cavitating flows in diesel injectors. *Atom. Sprays* **6**, 709–726.

Chen, Y. L. & Heister, S. D. 1996b Modeling hydrodynamic nonequilibrium in cavitating flows. *J. Fluids Engng: Trans. ASME* **118**, 172–178.

Chesters, A. K. & Hofman, G. 1982 Bubble coalescence in pure liquids. *Appl. Sci. Res.* **38**, 353–361.

Delannoy, Y. & Kueny, J. L. 1990 Two phase flow approach in unsteady cavitation modelling. In *Cavitation and Multiphase Flow Forum, ASME FED*, pp. 153–158.

Dukowicz, J. K. 1980 A particle-fluid numerical model for liquid sprays. *J. Comput. Phys.* **33**, 229.

Dumont, N., Simonin, O. & Habchi, C. 2001 Numerical simulation of cavitating flows in diesel injectors by a homogeneous equilibrium modeling approach. In *Proc. CAV2001, Fourth Intl Symp. Cavitation, Pasadena, CA* (ed. C. E. Brennen). California Institute of Technology.

Farrell, K. J. 2003 Eulerian/Lagrangian analysis for the prediction of cavitation inception. *J. Fluids Enng: Trans. ASME* **125**, 46–52.

Feng, Z. G. & Michaelides, E. E. 2001 Drag coefficients of viscous spheres at intermediate and high Reynolds numbers. *J. Fluids Engng: Trans. ASME* **123**, 841–849.

Fox, F. E. & Herzfeld, K. F. 1954 Gas bubbles with organic skin as cavitation nuclei. *J. Acoust. Soc. Am.* **26**, 984–989.

Gavaises, M. & Giannadakis, E. 2004 Modelling of cavitation in large-scale diesel injector nozzles. In *Proc. 20th Annu Conf. Liquid Atom. Spray Systems (ILASS-Europe), Nottingham, UK, 6–8 September* (ed. B. J. Azzopardi), pp. 159–164. School of Chemical, Environmental and Mining Enginnering, University of Nottingham.

GAVAISES, M., PAPOULIAS, D., ANDRIOTIS, A., GIANNADAKIS, E. & THEODORAKAKOS, A. 2007 Link between cavitation development and erosion damage in Diesel fuel injector nozzles. *SAE Paper* 2007-01-0246.

GIANNADAKIS, E. 2005 Modelling of cavitation in automotive fuel injector nozzles. PhD thesis, Imperial College, University of London, London, UK.

GIANNADAKIS, E., GAVAISES, M., ROTH, H. & ARCOUMANIS, C. 2004 Cavitation modelling in single-hole diesel injector based on Eulerian–Lagrangian approach. In *Proc. THIESEL Intl Conf. Thermo- Fluid Dyn. Processes Diesel Engines, Valencia, Spain*, pp. 47–60. La Editorial de la UPV.

GIANNADAKIS, E., PAPOULIAS, D., GAVAISES, M., ARCOUMANIS, C., SOTERIOU, C. & TANG, W. 2007 Evaluation of the predictive capability of diesel nozzle cavitation models. *SAE Paper* 2007-01-0245.

GINDROZ, B. & BILLET, M. L. 1998 Influence of the nuclei on the cavitation inception for different types of cavitation on ship propellers. *J. Fluids Engng: Trans. ASME* **120**, 171–178.

GONEY, K. H. & CORRADINI, M. L. 2000 Isolated effects of ambient pressure, nozzle cavitation and hole inlet geometry on diesel injection spray characteristics. *SAE Paper* 2000-01-2043.

GROGGER, H. A. & ALAJBEGOVIC, A. 1998 Calculation of the cavitating flow in venturi geometries using two fluid model. In *Proc. FEDSM'98 — 1998 ASME Fluid Engng Div. Summer Meeting, Washington, DC*.

HARVEY, E. N., BARNES, D. K., MCELROY, W. D., WHITELEY, A. H., PEASE, D. C. & COOPER, K. W. 1944 Bubble formation in animals. I. Physical factors. *J. Cell. Comp. Physiol.* **24**, 1–22.

HE, L. & RUIZ, F. 1995 Effect of cavitation on flow and turbulence in plain orifices for high-speed atomization. *Atom. Sprays* **5**, 569–584.

HENRY, M. E. & COLLICOTT, S. H. 2000 Visualization of internal flow in a cavitating slot orifice. *Atom. Sprays* **10**, 545–563.

HINZE, J. O. 1975 *Turbulence*, p. 309. McGraw-Hill.

HSIAO, C.-T., CHAHINE, G. L. & LIU, H. L. 2000 Scaling effect on bubble dynamics in a tip vortex flow: prediction of cavitation inception and noise. *Rep.* 98007-1, Dynaflow Inc, Jessup, MD, USA.

HSIAO, C.-T., CHAHINE, G. L. & LIU, H. L. 2003 Scaling effect on prediction of cavitation inception in a line vortex flow. *J. Fluids Engng: Trans. ASME* **125**, 53–60.

JOHNSON, V. E. & HSIEH, T. 1966 The influence of the trajectories of gas nuclei on cavitation inception. In *Proc. Sixth Symp. Naval Hydrodyn.*, pp. 163–179. Office of Naval Research, Washington, DC.

KAMP, A. M., CHESTERS, A. K., COLIN, C. & FABRE, J. 2001 Bubble coalescence in turbulent flows: a mechanistic model for turbulence-induced coalescence applied to microgravity bubbly pipe flow. *Intl J. Multiphase Flow* **27**, 1363–1396.

KINJO, T. & MATSUMOTO, M. 1998 Cavitation processes and negative pressure. *Fluid Phase Equil.* **144**, 343–350.

KODAMA, Y., TAKE, N., TAMIYA, S. & KATO, H. 1981 The effect of nuclei on the inception of bubble and sheet cavitation on axisymmetric-bodies. *J. Fluids Engng: Trans. ASME* **103**, 557–563.

KÖNIG, G. & BLESSING, M. 2000 Database of cavitation effects in nozzles for model verification: geometry and pressure effects on cavitating nozzle flow. DaimlerChrysler AG.

KUBOTA, A., KATO, H. & YAMAGUCHI, H. 1992 A new modelling of cavitating flows: a numerical study of unsteady cavitation on a hydrofoil section. *J. Fluid Mech.* **240**, 59–96.

LAÍN, S., BRÖDER, D., SOMMERFELD, M. & GÖZ, M. F. 2002 Modelling hydrodynamics and turbulence in a bubble column using the Euler-Lagrange procedure. *Intl J. Multiphase Flow* **28**, 1381–1407.

LIU, Z. H. & BRENNEN, C. E. 1998 Cavitation nuclei population and event rates. *J. Fluids Engng: Trans. ASME* **120**, 728–737.

MARCER, R., LE COTTIER, P., CHAVES, H., ARGUEYROLLES, B., HABCHI, C. & BARBEAU, B. 2000 A validated numerical simulation of diesel injector flow using a VOF method. *SAE Paper* 2000-01-2932.

MARCER, R. & LEGOUEZ, J. M. 2001 Simulation of unsteady cavitating flows in diesel injector with an improved VOF method. In *Proc. ILASS-EUROPE, Zurich, Switzerland* (ed. B. Ineichen). I.C. Engines and Combustion Laboratory, ETH, Zurich.

Martínez-Bazán, C., Montañés, J. L. & Lasheras, J. C. 1999*a* On the breakup of an air bubble injected into a fully developed turbulent flow. Part 1. Breakup frequency. *J. Fluid Mech.* **401**, 157–182.

Martínez-Bazán, C., Montañés, J. L. & Lasheras, J. C. 1999*b* On the breakup of an air bubble injected into a fully developed turbulent flow. Part 2. Size PDF of the resulting daughter bubbles. *J. Fluid Mech.* **401**, 183–207.

Maxey, M. R. & Riley, J. J. 1983 Equation of motion for a small rigid sphere in a nonuniform flow. *Phys. Fluids* **26**, 883–889.

Meyer, R. S., Billet, M. L. & Holl, J. W. 1992 Freestream nuclei and traveling-bubble cavitation. *J. Fluids Engng: Trans. ASME* **114**, 672–679.

Michaelides, E. E. 1997 Review: the transient equation of motion for particles, bubbles, and droplets. *J. Fluids Engng: Trans. ASME* **119**, 233–247.

Michaelides, E. E. 2003 Hydrodynamic force and heat/mass transfer from particles, bubbles, and drops: the Freeman scholar lecture. *J. Fluids Engng: Trans. ASME* **125**, 209–238.

Milton, S. G. & Arakeri, V. H. 1992 Studies on cavitation inception process in separated flows. *J. Fluids Engng: Trans. ASME* **114**, 85–92.

Mørch, K. A. 2000 Cavitation nuclei and bubble formation: a dynamic liquid–solid interface problem. *J. Fluids Engng: Trans. ASME* **122**, 494–498.

Moss, W. C., Levantin, J. L. & Szeri, A. J. 2000 A new damping mechanism in strongly collapsing bubbles. *Proc. R. Soc. Lond.* A **456**, 2983–2994.

Nurick, W. H. 1976 Orifice cavitation and its effects on spray mixing. *J. Fluids Engng* **98**, 681–687.

Papoulias, D., Giannadakis, E., Mitroglou, N., Gavaises, M. & Theodorakakos, A. 2007 Cavitation in fuel injection systems for spray guided direct injection gasoline engines. *SAE Paper* 2007-01-1418.

Plesset, M. S. & Prosperetti, A. 1977 Bubble dynamics and cavitation. *Annu. Rev. Fluid Mech.* **9**, 145–185.

Press, W. H., Teukolsky, S. A., Vetterling, W. T. & Flannery, B. P. 1992 *Numerical Recipes in Fortran 77*. Cambridge University Press.

Press, W. H., Teukolsky, S. A., Vetterling, W. T. & Flannery, B. P. 1996 *Numerical Recipes in Fortran 90*. Cambridge University Press.

Rood, E. P. 1991 Mechanisms of cavitation inception: review. *J. Fluids Engng: Trans. ASME* **113**, 163–175.

Roth, H. 2004 Experimental and computational investigation of cavitation in diesel injector nozzles. PhD thesis, Imperial College, University of London, London, UK.

Roth, H., Gavaises, M. & Arcoumanis, C. 2002 Cavitation initiation, its development and link with flow turbulence in diesel injector nozzles. *SAE Trans. J. Engines* **111–3**, 561–580.

Roth, H., Giannadakis, E., Gavaises, M., Arcoumanis, C., Omae, K., Sakata, I., Nakamura, M. & Yanagihara, H. 2005 Effect of multi-injection strategy on cavitation development in diesel injector nozzle holes. *SAE Trans. J. Engines* **114–3**, 1029–1045.

Rusche, H. & Issa, R. 2000 The effect of voidage on the drag force on particles, droplets and bubbles in dispersed two-phase flow. In *Proc. 2nd Japanese–European Two-Phase Flow Gp Meeting, Tsukuba, Japan*.

Sauer, J. & Schnerr, G. H. 2000 Unsteady cavitating flow: a new cavitation model based on a modified front capturing method and bubble dynamics. In *Proc. FEDSM'00 — 2000 ASME Fluid Engng Div. Summer Meeting, Boston, MA*.

Schmidt, D. P. & Corradini, M. L. 2001 The internal flow of diesel fuel injector nozzles: a review. *Intl J. Engine Res.* **2**, 1–22.

Schmidt, D. P., Rutland, C. J. & Corradini, M. L. 1997 A numerical study of cavitating flow through various nozzle shapes. *SAE Paper* 971597.

Schmidt, D. P., Rutland, C. J. & Corradini, M. L. 1999 A fully compressible, two-dimensional model of small, high-speed, cavitating nozzles. *Atom. Sprays* **9**, 255–276.

Schnerr, G. H. & Sauer, J. 2001 Physical and numerical modeling of unsteady cavitation dynamics. In *Proc. ICMF 2001: Fourth Intl Conf. Multiphase Flows, New Orleans, LA*.

Shyy, W., Thakur, S., Ouyang, H., Liu, J. & Blosch, E. 1997 *Computational Techniques for Complex Transport Phenomena*. Cambridge University Press.

Singhal, A. K., Athavale, M. M., Li, H. Y. & Jiang, Y. 2001 Mathematical basis and validation of the full cavitation model. In *Proc. FEDSM'01 — 2001 ASME Fluid Engng Div. Summer Meeting, New Orleans, LA.*

Singhal, A. K., Athavale, M. M., Li, H. Y. & Jiang, Y. 2002 Mathematical basis and validation of the full cavitation model. *J. Fluids Engng: Trans. ASME* **124**, 617–624.

Soteriou, C., Andrews, R. J. & Smith, M. 1995 Direct injection diesel sprays and the effect of cavitation and hydraulic flip on atomization. *SAE Paper* 950080.

Soteriou, C., Smith, M. & Andrews, R. J. 1998 Diesel injection: laser light sheet illumination of the development of cavitation in orifices. *IMechE Paper* C529/018/98.

Sou, A., Masaki, Y. & Nanajima, T. 2001 Numerical simulation of transient cavitating flow in a spray nozzle. In *Proc. ILASS-Asia*, Busan, Korea.

Sou, A., Nitta, S. & Nakajima, T. 2002 Bubble tracking simulation of cavitating flow in an atomization nozzle. In *Proc. FEDSM'02 — 2002 ASME Fluid Engng Div. Summer Meeting, Montreal, QC, Canada.*

Sridhar, G. & Katz, J. 1995 Drag and lift forces on microscopic bubbles entrained by a vortex. *Phys. Fluids* **7**, 389–399.

Tamaki, N., Shimizu, M. & Hiroyasu, H. 2001 Enhancement of the atomization of a liquid jet by cavitation in a nozzle hole. *Atom. Sprays* **11**, 125–137.

Temperley, H. N. V. & Trevena, D. H. 1994 Metastability of the liquid–vapor transition and related effects. *J. Stat. Phys.* **77**, 501–508.

Tamura, Y., Sugiyama, K. & Matsumoto, Y. 2001 Cavitating flow simulations based on the bubble dynamics. In *Proc. CAV2001: Fourth International Symposium on Cavitation, Pasadena, CA*, (ed. C. E. Brennen). California Institute of Technology.

Trevena, D. H. 1987 *Cavitation and Tension in Liquids.* Adam Hilger.

Vaidyanathan, R., Senocak, I., Wu, J. Y. & Shyy, W. 2003 Sensitivity evaluation of a transport-based turbulent cavitation model. *J. Fluids Engng: Trans. ASME* **125**, 447–458.

Vinogradova, O. I., Bunkin, N. F., Churaev, N. V., Kiseleva, O. A., Lobeyev, A. V. & Ninham, B. W. 1995 Submicrocavity structure of water between hydrophobic and hydrophilic walls as revealed by optical cavitation. *J. Colloid Interface Sci.* **173**, 443–447.

Wallis, G. B. 1969 *One-Dimensional Two-phase Flow*, p. 143. McGraw-Hill.

Walther, J., Schaller, J. K., Heinold, O., Kunzi, U. & Müller, D. 2001 Data base of structure and dynamic behavior of cavitation. Robert Bosch GmbH.

Walther, J., Schaller, J. K., Wirth, R. & Tropea, C. 2000 Investigation of internal flow in transparent diesel injection nozzles using fluorescent particle image velocimetry (FPIV). In *Proc. ICLASS, Pasadena, CA* (ed. N. Chigier), pp. 300–307.

van Wijngaarden, L. 1976 Hydrodynamic interaction between bubbles in a liquid. *J. Fluid Mech.* **77**, 27–44.

Xiao, C. & Heyes, D. M. 2002 Cavitation in stretched liquids. *Proc. R. Soc. Lond.* A **458**, 889–910.

Yakhot, V., Orszag, S. A., Thangam, S., Gatski, T. B. & Speziale, C. G. 1992 Development of turbulence models for shear flows by a double expansion technique. *Phys. Fluids* A **4**, 1510–1520.

Yuan, W., Sauer, J. & Schnerr, G. H. 2000 Modeling and computation of unsteady cavitation flows in injection nozzles. In *1st Intl Colloq. Microhydrodynamics*, Paris, France.

Yuan, W. & Schnerr, G. H. 2001 Cavitation in injection nozzles: effect of injection pressure fluctuations. In *Proc. CAV2001: Fourth Intl Symp. Cavitation, Pasadena, CA* (ed. C. E. Brennen). California Institute of Technology.